The Astrophysical Journal, 945:46 (20pp), 2023 March 1 https://doi.org/10.3847/1538-4357/aca80a

Inferencing Progenitor and Explosion Properties of Evolving Core-collapse Supernovae from Zwicky Transient Facility Light Curves

Bhagya M. Subrayan[1,8], Dan Milisavljevic[1,2], Takashi J. Moriya[3,4], Kathryn E. Weil[1], Geoffery Lentner[1], Mark Linvill[1], John Banovetz[1,5], Braden Garretson[1], Jack Reynolds[1], Niharika Sravan[6], Ryan Chornock[7], and Raffaella Margutti[7]

[1] Department of Physics and Astronomy, Purdue University, 525 Northwestern Avenue, West Lafayette, IN 47907, USA
[2] Integrative Data Science Initiative, Purdue University, West Lafayette, IN 47907, USA
[3] National Astronomical Observatory of Japan, National Institutes of Natural Sciences, 2-21-1 Osawa, Mitaka, Tokyo 181-8588, Japan
[4] School of Physics and Astronomy, Faculty of Science, Monash University, Clayton, Victoria 3800, Australia
[5] Brookhaven National Laboratory, Upton, New York, USA
[6] California Institute of Technology, Pasadena, CA 91125, USA
[7] Department of Astronomy, University of California, Berkeley, CA 94720-3411, USA
Received 2022 July 18; revised 2022 November 11; accepted 2022 November 23; published 2023 March 6

Abstract

We analyze a sample of 45 Type II supernovae from the Zwicky Transient Facility public survey using a grid of hydrodynamical models in order to assess whether theoretically driven forecasts can intelligently guide follow-up observations supporting all-sky survey alert streams. We estimate several progenitor properties and explosion physics parameters, including zero-age main-sequence (ZAMS) mass, mass-loss rate, kinetic energy, ^{56}Ni mass synthesized, host extinction, and the time of the explosion. Using complete light curves we obtain confident characterizations for 34 events in our sample, with the inferences of the remaining 11 events limited either by poorly constraining data or the boundaries of our model grid. We also simulate real-time characterization of alert stream data by comparing our model grid to various stages of incomplete light curves ($\Delta t < 25$ days, $\Delta t < 50$ days, all data), and find that some parameters are more reliable indicators of true values at early epochs than others. Specifically, ZAMS mass, time of the explosion, steepness parameter β, and host extinction are reasonably constrained with incomplete light-curve data, whereas mass-loss rate, kinetic energy, and ^{56}Ni mass estimates generally require complete light curves spanning >100 days. We conclude that real-time modeling of transients, supported by multi-band synthetic light curves tailored to survey passbands, can be used as a powerful tool to identify critical epochs of follow-up observations. Our findings are relevant to identifying, prioritizing, and coordinating efficient follow-up of transients discovered by the Vera C. Rubin Observatory.

Unified Astronomy Thesaurus concepts: Supernovae (1668); Surveys (1671); Hydrodynamical simulations (767); Type II supernovae (1731)

1. Introduction

The upcoming Legacy Survey of Space and Time (LSST) to be conducted by the Vera C. Rubin Observatory is highly anticipated to revolutionize time-domain astronomy (LSST Science Collaboration et al. 2009). Its sensitivity (∼24 mag), six broadband filters (*u-g-r-i-z-y*), regular southern-sky patrolling (cadences anticipated between hourly and every few days; LSST Science Collaboration et al. 2017), and prompt reporting of transient activity (latency of ≈60 s from exposure readout to alert distribution) will provide opportunities to discover and investigate millions of supernovae (SNe) over its planned 10 yr lifetime (Ivezić et al. 2019).

However, managing the massive data sets associated with LSST will be demanding. It will produce ∼20 TB of raw images every single night, which will be processed rapidly via template subtraction to send out real-time alerts of residual source variability (approximately 10 million alerts nightly). Moreover, because LSST photometry alone will generally be insufficient to adequately investigate the transients it will discover (Alves et al. 2022), the survey's success will be partially dependent on other telescopes for supporting observations (see, e.g., Najita et al. 2016), with electromagnetic and multi-messenger facilities (Huerta et al. 2019).

LSST Corporation (LSSTC) architects along with emerging alert stream data brokers are developing the processes, cyberinfrastructure, and software needed to confront this challenge and help manage upcoming LSST discoveries (Borne 2008; Narayan et al. 2018). Data brokers utilize transient classification methods that often employ machine learning (Möller & de Boissiere 2020; Förster et al. 2021; Sooknunan et al. 2021; García-Jara et al. 2022). Current data brokers include ALeRCE[9] (Sánchez-Sáez et al. 2021), ANTARES[10] (Matheson et al. 2021), Lasair[11] (Smith 2019), MARS,[12] and FINK[13] (Möller et al. 2021), Babamul, and PITT-Google. These data brokers are taking on different responsibilities to promptly process, value-add, cross-reference, and classify survey alert streams, which in turn permits users to filter and prioritize targets.

[8] Corresponding author.

[9] Automatic Learning for the Rapid Classification of Events, http://alerce.science/.
[10] Arizona-NOIRLab Temporal Analysis and Response to Events System, https://antares.noirlab.edu/.
[11] https://lasair.roe.ac.uk/
[12] Make Alerts Really Simple, https://Mars.lco.global/.
[13] https://fink-broker.org/

Working downstream of these data brokers are additional services to coordinate follow-up observations, including Target and Observation Managers (TOMs) that permit observers to sort through broker alert streams to plan and trigger follow-up (Street et al. 2018). TOMs have some level of automation, but generally rely largely on humans to make decisions about target prioritization and coordination. The Recommender Engine For Intelligent Transient Tracking (REFITT; Sravan et al. 2020) is an attempt to completely automate transient follow-up as an Object Recommender for Augmentation and Coordinating Liaison Engine (ORACLE). REFITT uses data from surveys to predict the light-curve evolution of transients, prioritizes events based on confidence in its prediction, and finally makes recommendations to observers on targets that need follow-up, specific to their observing facility and coordinated among all observing agents.

To date, decisions about which transients to prioritize for follow-up observations with supporting facilities are generally *data driven,* i.e., based on comparisons to data sets of previously observed events. In this paper, we explore the feasibility of guiding the follow-up of core-collapse supernovae (CCSNe) using parameters of *theoretically driven* forecasts. Our expectation is that prioritizing the underlying physics of transients will make it possible to (1) rapidly recognize transients of desired physical parameter spaces, and (2) identify information-rich epochs in transient evolution for efficient follow-up with limited facilities.

To this end, in this paper we characterize a sample of 45 light curves of Type II SNe using publicly available data from the Zwicky Transient Facility (ZTF; Bellm et al. 2019) survey with a grid of theoretical hydrodynamical models spanning various progenitor properties (zero-age main-sequence (ZAMS) mass, mass-loss history, etc.) and explosion physics (e.g., kinetic energy, ^{56}Ni synthesized). We compare results between model fits with both complete and incomplete light curves in order to assess whether theoretically driven forecasts can intelligently guide follow-up observations supporting all-sky survey alert streams. ZTF data is used because, among currently operating all-sky surveys, which include ATLAS[14] (Tonry et al. 2018) and ASAS-SN[15] (Shappee et al. 2014), ZTF's functioning alert stream best mimics LSST data flow, but at a more manageable scale (Masci et al. 2019). Although ZTF's cadence, depth, and filters differ from those of LSST, it still serves as an excellent testing ground for developing the infrastructure and software that LSST will require as it starts operating.

The paper is organized as follows: Section 2 describes the treatment of ZTF data in multiple passbands with forced photometry and extinction. In Section 3, we describe our hydrodynamical models with circumstellar material (CSM) structure constructed using the stellar evolutionary code KEPLER and the radiative transfer code STELLA. Section 4 outlines the results from our fitting method and trends in the parameters derived from the fits, and Section 5 describes our real-time fitting analysis of ZTF events and an assessment of how model parameters evolve as a function of time. The implications and utility of this work in view of current and upcoming all-sky surveys, including LSST are discussed in Section 6.

[14] Asteroid Terrestrial-impact Last Alert System.
[15] All-Sky Automated Survey for Supernovae.

2. Survey Data from ZTF

We used data from the public ZTF alert stream, available as photometry in the ztf-*g* and ztf-*r* passbands. We selected 45 ZTF events from Garretson et al. (2021) that are spectroscopically classified as Type II or IIP (Table 1). For the events that were classified as Type II, we confirmed that the light curves clearly demonstrated some portion of the plateau phase through visual inspection, differentiating them from Type IIL SNe. The events span the first 4 yr of the ZTF survey starting from 2018 to 2021. All events in this sample have a minimum of five detections, as defined below, in each of the ztf-*g* and ztf-*r* passbands. We treat this as a representative test sample as the light curves represent a variety of phases in evolution, reasonably span expected redshifts of the survey ($0.010 < z < 0.055$), and span peak apparent magnitudes approximately between 18 and 20 mag.

We utilize point-spread-function fit photometry measurements using difference imaging as provided by the ZTF forced-photometry service (IRSA 2022). Complete light curves were constructed from the differential flux measurements (*forcediffimflux* and *forcediffimfluxunc*) that the service returns in each band along with upper limits. A signal-to-noise threshold $= 3$ and a signal-to-noise ratio $= 5$ were used to declare the measurements as a detection versus an upper limit (Masci et al. 2019). The photometric zero-points in each passband were used to calculate the differential magnitudes.

We use the redshift reported by the Transient Name Server (TNS) to calculate the distance modulus using `astropy` (Astropy Collaboration et al. 2013, 2018) for every ZTF event assuming standard flat Lambda cold dark matter (ΛCDM) cosmology model with $H_0 = 70\,\mathrm{km\,Mpc^{-1}\,s^{-1}}$ and $\Omega_0 = 0.3$. The measurements are corrected for Milky Way extinction using dust maps as prescribed by Schlegel et al. (1998) for each passband, assuming an $R_V = 3.1$. In our analysis, for each ZTF event, we only use measurements up to 150 days in the rest frame from the first detection. We do not account for cosmological K-corrections in this work since we use a sample of low-redshift events. However, because LSST is expected to discover events at higher redshifts, K-corrections for a similar analysis of LSST events would be non-negligible.

3. Model Fitting

3.1. Model Grid Using STELLA

The hydrodynamic models used in this work are specific to Type IIP, constructed using the multigroup radiation hydrodynamics code STELLA (Blinnikov et al. 1998, 2000, 2006; Moriya et al. 2017, 2018; Ricks & Dwarkadas 2019). In this work, our models have the following parameters: ZAMS mass, the kinetic energy of the explosion (E_k), mass-loss rate ($\dot{M}$), steepness of velocity law (β) associated with the stellar wind, and ^{56}Ni mass synthesized. The model parameters along with their corresponding values in the grid are described in Table 2. Red supergiant (RSG) pre-supernova (SN) progenitors from Sukhbold et al. (2016) were used, which were calculated using the KEPLER code (Weaver et al. 1978), with physics previously discussed (e.g., Woosley et al. 2002). A neutron star remnant mass of 1.4 $M_\odot$ is assumed and the SN explosions are triggered by putting thermal energy above the mass cut. ^{56}Ni is assumed to be uniformly mixed up to half of the hydrogen-rich envelope in the mass coordinate.

Table 1
ZTF Events in This Paper

ZTF ID	TNS Classification	TNS Name	R.A. (J2000)	Decl. (J2000)	Redshift (z)	No. of g-band Detections	No. of r -band Detections
ZTF18abcpmwh[a]	IIP	SN 2018cur	12:59:09.12	+37:19:00.19	0.015	8(12)	8(40)
ZTF18acbvhit	II	SN 2018hle	3:39:28.11	−13:07:02.50	0.014	16	15
ZTF18acbwasc[b]	IIP	SN 2018hfc	11:01:58.61	+45:13:39.26	0.020	51	65
ZTF18acrtvmm[a]	II	SN 2018jfp	3:17:56.27	−0:10:10.82	0.023	17	20(2)
ZTF18acuqskr	II	SN 2018jrb	8:09:33.69	+15:31:10.55	0.045	7	10
ZTF19aakiyed	II	SN 2019awk	15:07:02.58	+61:13:42.37	0.044	17	23
ZTF19aaqdkrm	II	SN 2019dod	13:25:49.97	+34:29:43.58	0.034	27	30
ZTF19aauqwna	IIP	SN 2019fem	19:44:46.13	+44:42:49.13	0.041	20	47
ZTF19aavbkly	IIP	SN 2019fmv	12:29:33.80	+35:46:12.15	0.041	31	29
ZTF19aavhblr	II	SN 2019fuo	15:31:43.38	+16:42:49.30	0.050	19	27
ZTF19aavkptg	IIP	SN 2019gqs	11:36:15.78	+49:09:12.55	0.038	30	22
ZTF19abguqsi	II	SN 2019lsh	22:52:58.52	+0:26:50.53	0.052	14	20
ZTF19abhduuo[b]	II	SN 2019lre	1:58:50.79	−9:35:05.65	0.018	14	16
ZTF19abiahko	IIP	SN 2019lsj	19:36:59.13	−11:57:13.63	0.023	8	11
ZTF19abqyouo[b]	IIP	SN 2019pbk	7:46:23.89	+64:13:23.79	0.045	11	13
ZTF19abvbrve	IIP	SN 2019puv	19:12:36.67	−19:25:01.67	0.020	14	42
ZTF19acbvisk[a]	II	SN 2019rms	9:00:45.39	+19:44:42.32	0.037	19	37(1)
ZTF19ackjvtl[b]	IIP	SN 2019uwd	13:16:20.75	+30:40:48.72	0.019	53	99
ZTF19acmwfli[b]	II	SN 2019tza	13:14:04.68	+59:15:04.91	0.028	39	59
ZTF19acszmgx	II	SN 2019vew	5:27:49.43	−5:21:39.88	0.042	22	22
ZTF20aahqbun	II	SN 2020alg	14:27:10.55	+35:55:20.22	0.028	26	41
ZTF20aamlmec	II	SN 2020chv	7:46:27.78	+1:57:34.73	0.034	8	9
ZTF20aamxuwl	II	SN 2020ckv	11:03:26.48	−1:32:27.04	0.037	13	12
ZTF20aatqgeo	II	SN 2020fcx	13:40:10.01	+23:20:29.56	0.032	25	16
ZTF20aatqidk	II	SN 2020fbj	12:47:47.03	+22:17:10.44	0.034	26	29
ZTF20aaullwz	II	SN 2020fch	11:33:24.03	−9:20:55.94	0.027	12	10
ZTF20aausahr	II	SN 2020hgm	8:31:22.09	+49:13:35.43	0.043	9	10
ZTF20aazcnrv	II	SN 2020jjj	14:31:19.63	−25:39:31.04	0.023	12	13
ZTF20aazpphd	II	SN 2020jww	16:10:51.58	+27:09:42.02	0.046	36	43
ZTF20abekbzp	II	SN 2020meu	15:34:44.68	+6:38:53.35	0.041	9	11
ZTF20abuqali	II	SN 2020rht	2:30:17.30	+28:36:02.64	0.040	13	12
ZTF20abwdaeo[b]	II	SN 2020rvn	21:06:36.34	+17:59:34.86	0.021	28	29
ZTF20abyosmd[b]	II	SN 2020toc	8:28:30.14	+17:28:08.52	0.021	20	26
ZTF20acjqksf[b]	IIP	SN 2020tfb	6:08:52.14	−26:24:46.02	0.048	17	18
ZTF20acnvtxy[b]	IIP	SN 2020zkx	11:18:31.84	+6:44:28.84	0.030	10	13
ZTF20acptgfl	IIP	SN 2020zjk	5:22:00.02	−7:11:20.81	0.037	22	27
ZTF21aabygea[a]	II	SN 2021os	12:02:54.08	+5:36:53.15	0.019	31	49(2)
ZTF21aaevrjl	II	SN 2021arg	4:31:18.78	−10:23:46.95	0.031	14	15
ZTF21aafkktu	II	SN 2021avg	11:39:59.00	+14:31:40.65	0.031	31	32
ZTF21aafkwtk	II	SN 2021apg	13:41:19.24	+24:29:43.88	0.027	26	37
ZTF21aagtqpn[b,a]	II	SN 2021bkq	18:20:34.83	+40:56:36.28	0.036	33(4)	44(6)
ZTF21aaigdly[b]	II	SN 2021cdw	14:05:31.80	−25:21:54.51	0.040	17	28
ZTF21aaluqkp	II	SN 2021dhx	11:05:10.38	−15:21:10.13	0.025	34	25
ZTF21aamzuxi	II	SN 2021dvl	7:49:56.10	+71:15:42.11	0.034	27	29
ZTF21acchbmn	II	SN 2021zaa	23:46:41.12	+26:44:45.11	0.032	22	19

Notes.
[a] The reported number of measurements in the ztf-g and ztf-r passbands obtained within 150 days of the first detection, after running forced photometry for each ZTF event. Additional detections beyond 150 days not included in the analysis are quoted in parenthesis for each band.
[b] No upper-limit constraints before the first detection are available for informed priors on the date of the explosion.

Our hydrodynamical model grid also incorporates an associated circumstellar material (CSM) density structure attached to these RSG progenitors. The CSM density is given by

$$\rho_{\rm CSM}(r) = \frac{\dot{M}}{4\pi v_{\rm wind} r^2}, \quad (1)$$

where $\dot{M}$ is the mass-loss rate and $v_{\rm wind}$ is the velocity structure associated with the stellar wind. The radial dependency of $v_{\rm wind}$ is given by the velocity law

$$v_{\rm wind}(r) = v_0 + (v_\infty - v_0)\left(1 - \frac{R_0}{r}\right)^\beta, \quad (2)$$

where v_0 is the initial wind velocity with a value <0.01 km s^{-1}, v_∞ is the terminal wind velocity $= 10$ km s^{-1}, R_0 is the wind launching radius set to the photosphere of the star, and β is the steepness parameter that gives a measure of wind acceleration. RSG progenitors typically have $\beta > 2$, owing to the slower

Table 2
Prior Distribution on Physical Parameters Used in Our Sampling Method along with Values of the Parameters in Our Hydrodynamical Model Grid

Parameter	Hydrodynamical Model Values	In Steps	Prior Distribution	Units
$t_{\rm exp}$	...	...	$U(0,\ t_{\rm upper-limit})$	day
ZAMS	12–16	2	$N(14,\ 3) \in (12,\ 16)$	$M_{\odot}$
E_k	0.5–5.0	0.5	$N(1,\ 1) \in (0.5,\ 5)$	10^{51} erg
^{56}Ni	0.01–0.1	0.01 (0.001,0.2,0.3)	$N(0.05,\ 0.01) \in (0.001,\ 0.3)$	$M_{\odot}$
β	1–5	1	$N(3,\ 2) \in (1,\ 5)$	...
$-\log_{10}\dot{M}$	1–5	0.5	$U(4,\ 2) \in (5,\ 1)$	$M_{\odot}$ yr^{-1}
A_V	...	...	$N\,(\ln(0.05),\ 2) \in (10^{-4},\ 2)$	mag

Note. The "In Steps" values in parentheses for ^{56}Ni are the additional values for the parameters present in the model grid.

acceleration of the stellar winds (Mauron & Josselin 2011). A fixed CSM radius of 10^{15} cm is assumed in our models.

The RSG progenitors with associated CSM density structures were then exploded as thermal bombs with energies ranging from $0.5–5.0 \times 10^{51}$ erg using STELLA. The code calculates the resulting light curve of the explosion following the evolution of spectral energy distributions (SEDs) with time at every epoch. The light curves in various passbands are obtained by convolving the ZTF filter transmission functions to the numerical SEDs. Our final grid varying the progenitor, explosion, and CSM properties is made up of 4206 unique models. A similar model grid used in this work can be found in Förster et al. (2018) for further reference. The full details of the numerical model grid will be presented in a separate paper (T. J. Moriya 2022, in preparation).

3.2. Fast Interpolation Method

Using Bayesian Inference methods requires the models to be finely sampled within the parameter space. However, because our model grid is neither complete nor uniform, a scale-independent fast interpolation process that can use a nonuniform grid of models was incorporated into our Monte Carlo sampling method following Förster et al. (2018) and Martinez et al. (2020). This allowed us to quickly interpolate between the models in the grid to sample any combination of values in the parameter space. For a given parameter vector $\boldsymbol{\theta}$, the method finds the closest models $\boldsymbol{\theta}_{\rm close}$ and weighs them appropriately using

$$m(t,\ \boldsymbol{\theta}) = \sum_{\boldsymbol{\theta}_i \in \boldsymbol{\theta}_{\rm close}} \hat{w}(\boldsymbol{\theta},\ \boldsymbol{\theta}_i) m(t,\ \boldsymbol{\theta}_i), \tag{3}$$

where $m(t,\ t_{\rm exp},\ \boldsymbol{\theta})$ is the magnitude for a given $\boldsymbol{\theta}$ at time t and the normalized weights are given by

$$\hat{w}(\boldsymbol{\theta},\ \boldsymbol{\theta}_i) = \frac{w(\boldsymbol{\theta},\ \boldsymbol{\theta}_i)}{\sum\limits_{\boldsymbol{\theta}_j \in \boldsymbol{\theta}_{\rm close}} w(\boldsymbol{\theta},\ \boldsymbol{\theta}_j)}, \tag{4}$$

where

$$w(\boldsymbol{\theta},\ \boldsymbol{\theta}_i) = \left(\prod_j |\theta^j - \theta_i^j| + \delta^j \right)^{-1}. \tag{5}$$

Equation (5) uses a very small vector $\boldsymbol{\delta}$ with the same units as $\boldsymbol{\theta}$, which ensures that the weights do not diverge when a given parameter combination exactly matches a model in the grid. This fast interpolation method can be used to calculate light curves for any combination of parameter vector θ bound by the limits of our model grid.

3.3. Date of the Explosion and Host Extinction

Along with fitting for the parameters of our models, we also fit for the date of the explosion and host extinction. The time of the explosion is calculated as the number of days before the first photometric measurement in each passband. We defined an informed prior distribution for the time of explosion leveraging the constraints given by the upper limits in each passband for each event. The priors are more constraining if the upper limits preceding the first detection are well defined. To calculate the approximate bounds of time of explosion priors, the deepest upper limit available before the first detection is identified. If no upper limits are available for an event, we allow a wider distribution for the prior.

Observed Type II SN light curves can be significantly affected by host extinction (Kasen & Woosley 2009; Kochanek et al. 2012; Mattila et al. 2012). We fit for total extinction in the visual band assuming a prior distribution listed in Table 2. We do this by simultaneously fitting the ztf-g and ztf-r passbands to infer host extinction. The derived extinction is used to calculate $E(B-V)$ for the host of each event assuming $R_V = 3.1$.

3.4. Nested Sampling Methods for Parameter Inference

We derive posterior distributions of the parameters involved using the python-based MIT-licensed Dynamic Nested Sampling package `dynesty` (Skilling 2004) that estimates the Bayesian target distributions. We assigned a combination of uniform and Gaussian distributions as our priors for different parameters. The prior distributions considered in this work are listed in Table 2. The likelihood function incorporates fast interpolation and evaluates how close the observations are with a sample model drawn. Using the above framework, multi-band ZTF observations in the ztf-g and ztf-r passbands in their absolute magnitudes are fit to the hydrodynamical models.

Nested sampling methods require all the samples to be identically and independently distributed random variables drawn from the prior distribution. We use a uniform sampling method widely used for dimensions <10 in the `dynesty` package (Skilling 2006). In the Bayesian framework, all of the inferences are contained in the final multidimensional posterior, which can be marginalized over each parameter to obtain constraints. The Bayesian evidence is represented by the overall normalization of this posterior. The nested sampling algorithm converges until the evidence has been estimated to the desired accuracy after accepting or rejecting the samples that are drawn from the prior distribution.

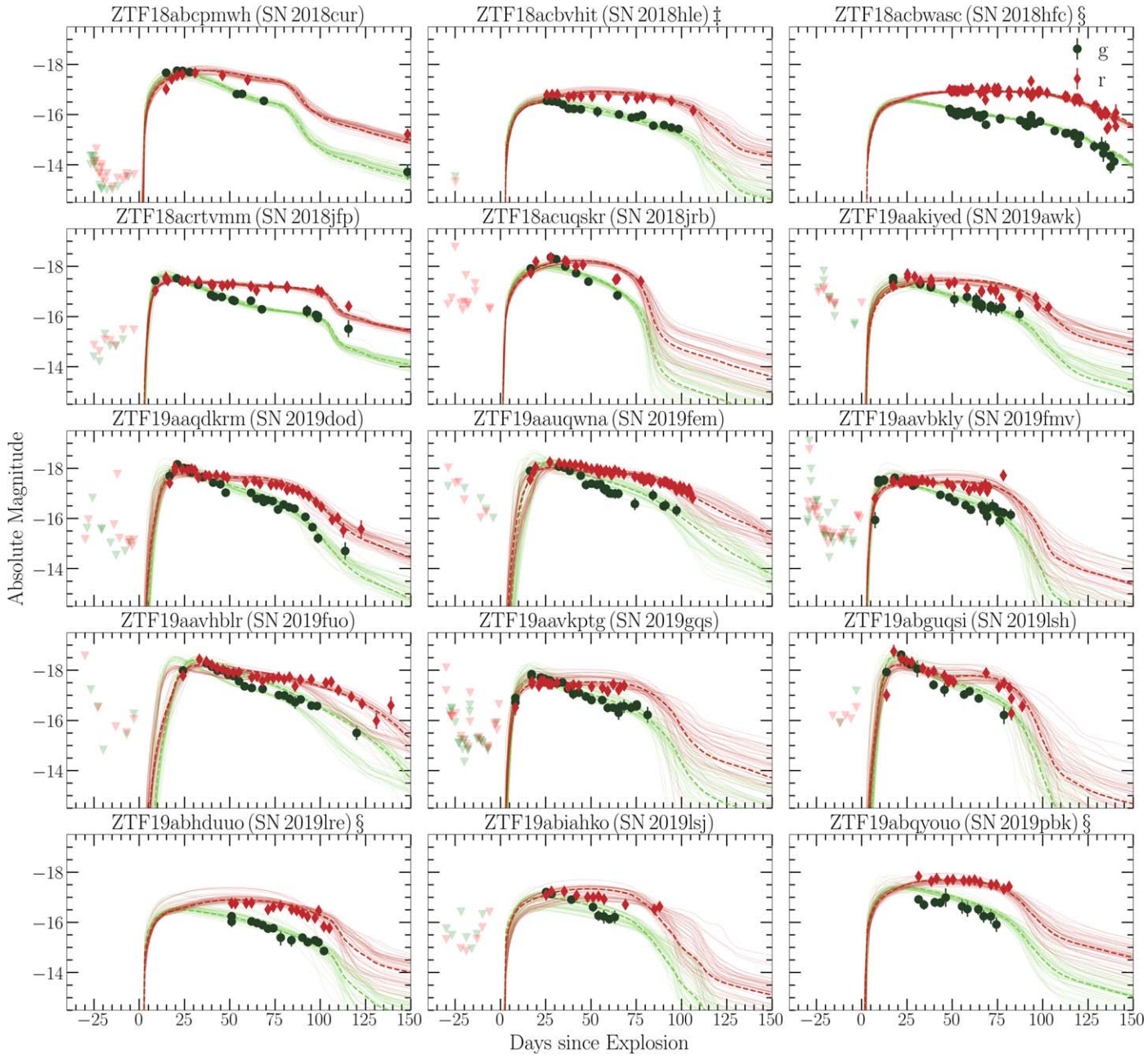

Figure 1. The observed ZTF light curves and our model fits plotted with respect to the derived time of the explosion. The family of light curves in each panel represents 150 models randomly sampled from the derived posterior probability distribution in individual bands. respectively. The dashed curve represents the best-fit model for each ZTF event. The upper limits before the first detection that are used to constrain the date of the explosion are plotted. The median values and their 1σ uncertainty for the parameters are listed in Table 3. ZTF events with no upper limits and poorly constraining rise data are flagged with §. ZTF events whose fits approached the model boundaries are flagged with ‡. Additional plots for the remaining ZTF events listed in Table 1 are provided in the Appendix.

4. Parameter Inference and Trends of Complete Light Curves

Using our Bayesian inference procedure to fit all ZTF events with our model grid, we derived the posterior probability distribution for all parameters of each Type II SNe. Our models were fit confidently to 34 events. The fits for the remaining 11 events were limited by poor upper limits prior to first detection (flagged with §) and the hydrodynamical model grid boundaries (flagged with ‡). Figure 1 shows the samples of the posterior probability distributions for the first 15 ZTF events. The light-curve fits for the remaining events are plotted in an extended version of Figure 1 in the Appendix. The observed data points are shifted with respect to the inferred date of the explosion and corrected for host extinction derived from the fits. The uncertainty in the host extinction and the date of the explosion are not represented in Figure 1. The dashed line in each passband represents the best-fit model. Table 3 lists the inferred median values for the seven parameters with their 16th and 84th percentile confidence regions. We note that these 1σ uncertainties of the parameters only reflect how well the model fits the observed data and do not take into account any uncertainties related to the assumptions used to create the model grid itself. Representative corner plots of posterior probability distributions are shown in the Appendix.

Table 3
Median Values from the Posterior Distribution with 1σ Uncertainty When Fitted with All Data from the Events

ZTF ID	ZAMS ($M_\odot$)	E_k (10^{51} erg)	$-\log_{10}\dot{M}$ ($M_\odot$ yr^{-1})	$M_{\rm Ni56}$ ($M_\odot$)	$t_{\rm exp}$ (days)	β	A_V (mag)
ZTF18abcpmwh	$15.77^{+0.20}_{-1.39}$	$1.67^{+0.35}_{-0.29}$	$4.09^{+0.38}_{-0.40}$	$0.07^{+0.02}_{-0.02}$	$14.81^{+1.88}_{-1.58}$	$2.56^{+1.20}_{-0.27}$	$0.23^{+0.11}_{-0.10}$
ZTF18acbvhit[b]	$13.35^{+1.68}_{-0.91}$	$0.51^{+0.02}_{-0.01}$	$4.00^{+0.09}_{-0.09}$	$0.04^{+0.01}_{-0.01}$	$25.54^{+3.93}_{-4.04}$	$3.98^{+0.09}_{-0.10}$	$0.31^{+0.09}_{-0.09}$
ZTF18acbwasc[b]	$12.47^{+0.40}_{-0.31}$	$0.52^{+0.01}_{-0.01}$	$4.22^{+0.35}_{-0.36}$	$0.10^{+0.005}_{-0.02}$	$48.48^{+1.06}_{-1.79}$	$3.06^{+0.17}_{-0.20}$	$0.02^{+0.02}_{-0.01}$
ZTF18acrtvmm	$12.86^{+0.80}_{-0.50}$	$0.99^{+0.04}_{-0.05}$	$2.43^{+0.15}_{-0.25}$	$0.10^{+0.04}_{-0.03}$	$8.81^{+0.75}_{-1.00}$	$3.64^{+0.14}_{-1.22}$	$0.03^{+0.03}_{-0.02}$
ZTF18acuqskr	$13.89^{+1.02}_{-0.98}$	$2.90^{+0.30}_{-0.39}$	$3.91^{+0.47}_{-0.45}$	$0.04^{+0.02}_{-0.02}$	$16.72^{+2.40}_{-2.38}$	$3.01^{+0.46}_{-0.45}$	$0.06^{+0.07}_{-0.04}$
ZTF19aakiyed	$14.85^{+1.04}_{-1.74}$	$1.02^{+0.21}_{-0.20}$	$3.75^{+0.52}_{-0.54}$	$0.06^{+0.02}_{-0.02}$	$17.29^{+3.22}_{-3.09}$	$2.93^{+0.82}_{-0.53}$	$0.10^{+0.10}_{-0.07}$
ZTF19aaqdkrm	$13.14^{+2.52}_{-0.81}$	$1.08^{+0.25}_{-0.28}$	$1.67^{+0.25}_{-0.21}$	$0.05^{+0.02}_{-0.01}$	$16.68^{+1.95}_{-2.88}$	$3.06^{+0.89}_{-1.20}$	$0.12^{+0.11}_{-0.08}$
ZTF19aauqwna	$13.71^{+1.17}_{-1.01}$	$1.19^{+0.30}_{-0.31}$	$1.32^{+0.26}_{-0.20}$	$0.08^{+0.02}_{-0.02}$	$16.29^{+6.28}_{-3.80}$	$3.03^{+0.55}_{-0.50}$	$0.05^{+0.07}_{-0.03}$
ZTF19aavbkly	$13.07^{+2.09}_{-0.75}$	$1.06^{+0.43}_{-0.21}$	$2.43^{+0.18}_{-0.25}$	$0.02^{+0.01}_{-0.01}$	$7.27^{+0.51}_{-0.82}$	$3.00^{+0.10}_{-0.10}$	$0.18^{+0.25}_{-0.10}$
ZTF19aavhblr	$13.46^{+1.36}_{-0.97}$	$0.86^{+0.28}_{-0.19}$	$1.09^{+0.41}_{-0.04}$	$0.07^{+0.02}_{-0.01}$	$24.13^{+4.25}_{-10.53}$	$2.98^{+0.49}_{-0.47}$	$0.05^{+0.09}_{-0.04}$
ZTF19aavkptg	$13.14^{+1.97}_{-0.80}$	$1.06^{+0.45}_{-0.26}$	$2.22^{+0.30}_{-0.20}$	$0.03^{+0.02}_{-0.02}$	$8.21^{+1.09}_{-1.40}$	$2.95^{+0.71}_{-0.50}$	$0.38^{+0.25}_{-0.17}$
ZTF19abguqsi	$12.57^{+1.02}_{-0.40}$	$1.24^{+0.73}_{-0.45}$	$1.51^{+0.06}_{-0.04}$	$0.01^{+0.01}_{-0.01}$	$13.71^{+0.88}_{-1.34}$	$3.00^{+0.45}_{-0.44}$	$0.17^{+0.19}_{-0.10}$
ZTF19abhduuo[b]	$12.95^{+0.85}_{-0.59}$	$0.52^{+0.05}_{-0.02}$	$4.00^{+0.08}_{-0.08}$	$0.03^{+0.01}_{-0.01}$	$51.02^{+5.20}_{-6.87}$	$3.97^{+0.47}_{-0.36}$	$0.79^{+0.17}_{-0.11}$
ZTF19abiahko	$13.11^{+0.92}_{-0.71}$	$0.75^{+0.32}_{-0.21}$	$3.99^{+0.11}_{-0.10}$	$0.02^{+0.01}_{-0.01}$	$25.15^{+7.76}_{-5.27}$	$3.99^{+0.10}_{-0.10}$	$0.54^{+0.23}_{-0.36}$
ZTF19abqyouo[b]	$12.98^{+1.36}_{-0.70}$	$1.39^{+0.15}_{-0.23}$	$3.95^{+0.58}_{-0.70}$	$0.06^{+0.02}_{-0.02}$	$31.37^{+3.16}_{-3.42}$	$3.00^{+0.85}_{-0.84}$	$0.09^{+0.09}_{-0.06}$
ZTF19abvbrve[a]	$12.85^{+1.59}_{-0.59}$	$0.51^{+0.02}_{-0.01}$	$3.56^{+0.57}_{-0.25}$	$0.06^{+0.02}_{-0.02}$	$8.27^{1.47}_{-1.16}$	$2.82^{+0.89}_{-0.43}$	$0.13^{+0.09}_{-0.07}$
ZTF19acbvisk	$13.82^{+0.77}_{-0.86}$	$0.54^{+0.07}_{-0.03}$	$1.63^{+0.41}_{-0.41}$	$0.10^{+0.02}_{-0.02}$	$20.02^{+9.31}_{-6.41}$	$3.11^{+0.48}_{-0.49}$	$0.02^{+0.03}_{-0.02}$
ZTF19ackjvtl[b]	$14.43^{+1.05}_{-1.26}$	$0.51^{+0.02}_{-0.01}$	$3.88^{+0.71}_{-0.80}$	$0.06^{+0.01}_{-0.00}$	$57.60^{+2.22}_{-1.99}$	$2.47^{+1.37}_{-0.83}$	$0.40^{+0.07}_{-0.07}$
ZTF19acmwfli	$13.34^{+2.19}_{-0.97}$	$1.01^{+0.06}_{-0.04}$	$3.82^{+0.71}_{-0.79}$	$0.04^{+0.01}_{-0.01}$	$24.75^{+2.12}_{-4.51}$	$2.69^{+1.07}_{-0.21}$	$0.21^{+0.10}_{-0.08}$
ZTF19acszmgx	$13.21^{+1.40}_{-0.86}$	$1.39^{+0.42}_{-0.40}$	$1.03^{+0.07}_{-0.03}$	$0.08^{+0.02}_{-0.02}$	$19.37^{+0.45}_{-0.88}$	$2.98^{+0.50}_{-0.47}$	$0.43^{+0.25}_{-0.36}$
ZTF20aahqbun	$15.39^{+0.51}_{-2.27}$	$0.58^{+0.05}_{-0.04}$	$3.01^{+1.11}_{-0.48}$	$0.06^{+0.01}_{-0.01}$	$27.73^{+1.51}_{-2.11}$	$2.55^{+1.20}_{-0.18}$	$0.17^{+0.07}_{-0.07}$
ZTF20aamlmec	$13.53^{+1.48}_{-1.01}$	$1.00^{+0.38}_{-0.26}$	$2.37^{+0.72}_{-0.40}$	$0.03^{+0.02}_{-0.02}$	$22.35^{+3.76}_{-3.56}$	$2.99^{+0.53}_{-0.49}$	$0.25^{+0.20}_{-0.16}$
ZTF20aamxuwl	$13.48^{+1.49}_{-1.00}$	$1.03^{+0.37}_{-0.28}$	$1.78^{+0.46}_{-0.39}$	$0.06^{+0.02}_{-0.01}$	$14.41^{+4.21}_{-3.18}$	$3.05^{+0.57}_{-0.54}$	$0.08^{+0.11}_{-0.06}$
ZTF20aatqgeo	$12.60^{+1.67}_{-0.43}$	$0.92^{+0.15}_{-0.25}$	$2.02^{+0.10}_{-0.06}$	$0.06^{+0.02}_{-0.02}$	$18.60^{+0.97}_{-1.54}$	$2.76^{+0.94}_{-0.40}$	$0.29^{+0.09}_{-0.13}$
ZTF20aatqidk	$13.81^{+1.21}_{-1.04}$	$0.61^{+0.05}_{-0.04}$	$2.67^{+0.37}_{-0.26}$	$0.10^{+0.04}_{-0.04}$	$16.88^{+2.47}_{-2.26}$	$3.52^{+0.26}_{-1.11}$	$0.03^{+0.04}_{-0.02}$
ZTF20aaullwz	$14.01^{+0.73}_{-0.69}$	$1.03^{+0.38}_{-0.08}$	$2.73^{+0.33}_{-0.28}$	$0.08^{+0.01}_{-0.02}$	$10.65^{+1.76}_{-1.94}$	$3.02^{+0.37}_{-0.35}$	$0.04^{+0.10}_{-0.03}$
ZTF20aausahr	$13.74^{+1.18}_{-1.02}$	$2.38^{+0.46}_{-0.34}$	$3.69^{+0.74}_{-1.01}$	$0.03^{+0.02}_{-0.02}$	$27.38^{+3.29}_{-3.29}$	$3.00^{+0.48}_{-0.47}$	$0.12^{+0.12}_{-0.08}$
ZTF20aazcnrv	$14.80^{+1.02}_{-1.61}$	$1.26^{+0.51}_{-0.39}$	$3.78^{+0.51}_{-0.52}$	$0.02^{+0.01}_{-0.01}$	$19.69^{+2.65}_{-2.43}$	$3.94^{+0.57}_{-0.27}$	$0.35^{+0.21}_{-0.20}$
ZTF20aazpphd	$13.73^{+0.82}_{-0.90}$	$1.00^{+0.03}_{-0.02}$	$1.86^{+0.33}_{-0.15}$	$0.10^{+0.03}_{-0.02}$	$13.94^{+1.67}_{-1.60}$	$3.08^{+0.45}_{-0.55}$	$0.02^{+0.03}_{-0.01}$
ZTF20abekbzp	$13.62^{+1.38}_{-1.05}$	$1.54^{+0.75}_{-0.46}$	$3.19^{+1.08}_{-0.78}$	$0.02^{+0.02}_{-0.02}$	$15.27^{+2.84}_{-3.34}$	$2.99^{+0.51}_{-0.49}$	$0.28^{+0.27}_{-0.18}$
ZTF20abuqali	$13.81^{+1.62}_{-1.22}$	$1.01^{+0.18}_{-0.15}$	$2.41^{+0.31}_{-0.33}$	$0.08^{+0.02}_{-0.02}$	$17.38^{+3.00}_{-2.96}$	$3.00^{+0.75}_{-0.56}$	$0.07^{+0.08}_{-0.05}$
ZTF20abwdaeo	$15.22^{+0.71}_{-1.95}$	$0.57^{+0.03}_{-0.03}$	$2.55^{+0.26}_{-0.27}$	$0.09^{+0.01}_{-0.02}$	$20.09^{+2.75}_{-2.49}$	$3.50^{+0.28}_{-1.08}$	$0.03^{+0.03}_{-0.02}$
ZTF20abyosmd[b]	$12.72^{+1.61}_{-0.51}$	$0.97^{+0.08}_{-0.25}$	$4.00^{+0.44}_{-0.44}$	$0.06^{+0.01}_{-0.01}$	$47.15^{+1.89}_{-3.01}$	$2.97^{+0.55}_{-0.49}$	$1.03^{+0.09}_{-0.11}$
ZTF20acjqksf[b]	$12.83^{+1.62}_{-0.59}$	$1.59^{+0.63}_{-0.45}$	$4.05^{+0.58}_{-0.63}$	$0.03^{+0.02}_{-0.02}$	$28.34^{+1.16}_{-1.99}$	$2.98^{+0.49}_{-0.47}$	$0.40^{+0.24}_{-0.22}$
ZTF20acnvtxy[b]	$13.32^{+1.49}_{-0.89}$	$1.38^{+0.59}_{-0.49}$	$3.89^{+0.65}_{-0.76}$	$0.03^{+0.02}_{-0.02}$	$54.43^{+3.58}_{-5.08}$	$3.00^{+0.44}_{-0.48}$	$0.98^{+0.28}_{-0.26}$
ZTF20acptgfl[a]	$12.94^{+0.42}_{-0.41}$	$0.52^{+0.02}_{-0.01}$	$3.97^{+0.15}_{-0.11}$	$0.05^{+0.01}_{-0.01}$	$19.41^{+2.76}_{-2.55}$	$3.00^{+0.10}_{-0.10}$	$0.08^{+0.07}_{-0.05}$
ZTF21aabygea	$15.96^{+0.03}_{-0.19}$	$0.57^{+0.02}_{-0.02}$	$3.76^{+0.18}_{-0.14}$	$0.05^{+0.02}_{-0.02}$	$9.84^{+0.87}_{-0.98}$	$3.75^{+0.05}_{-0.05}$	$0.02^{+0.02}_{-0.01}$
ZTF21aaevrjl	$13.72^{+1.19}_{-1.05}$	$1.42^{+0.76}_{-0.60}$	$4.00^{+0.10}_{-0.10}$	$0.02^{+0.02}_{-0.01}$	$14.82^{+3.13}_{-2.54}$	$3.00^{+0.10}_{-0.09}$	$0.81^{+0.30}_{-0.32}$
ZTF21aafkktu	$14.35^{+1.21}_{-1.29}$	$0.56^{+0.09}_{-0.05}$	$2.11^{+0.47}_{-0.40}$	$0.09^{+0.01}_{-0.01}$	$8.56^{+3.54}_{-2.31}$	$2.66^{+1.09}_{-0.33}$	$0.04^{+0.05}_{-0.03}$
ZTF21aafkwtk[a]	$14.36^{+1.12}_{-0.85}$	$0.51^{+0.01}_{-0.00}$	$2.75^{+0.35}_{-0.20}$	$0.04^{+0.01}_{-0.01}$	$13.52^{+1.84}_{-2.11}$	$2.78^{+0.74}_{-0.40}$	$0.05^{+0.04}_{-0.03}$
ZTF21aagtqpn	$12.11^{+0.17}_{-0.08}$	$1.44^{+0.10}_{-0.10}$	$4.04^{+0.45}_{-0.45}$	$0.10^{+0.002}_{-0.002}$	$19.70^{+1.21}_{-1.40}$	$2.50^{+1.23}_{-0.30}$	$0.04^{+0.04}_{-0.03}$
ZTF21aaigdly	$14.64^{+1.24}_{-1.76}$	$0.67^{+0.13}_{-0.07}$	$2.79^{+0.43}_{-0.26}$	$0.09^{+0.07}_{-0.06}$	$10.60^{+2.38}_{-2.14}$	$3.71^{+0.08}_{-1.24}$	$0.05^{+0.06}_{-0.04}$
ZTF21aaluqkp	$15.14^{+0.77}_{-2.06}$	$0.54^{+0.04}_{-0.02}$	$3.70^{+0.49}_{-0.42}$	$0.09^{+0.01}_{-0.03}$	$16.11^{+2.74}_{-2.75}$	$2.60^{+1.16}_{-0.19}$	$0.07^{+0.06}_{-0.04}$
ZTF21aamzuxi	$14.48^{+1.25}_{-1.36}$	$1.49^{+0.08}_{-0.09}$	$3.72^{+0.49}_{-0.51}$	$0.09^{+0.05}_{-0.06}$	$7.85^{+1.41}_{-1.31}$	$2.56^{+1.20}_{-0.23}$	$0.05^{+0.05}_{-0.04}$
ZTF21acchbmn	$14.14^{+1.62}_{-1.35}$	$1.51^{+0.13}_{-0.08}$	$2.17^{+0.32}_{-0.24}$	$0.09^{+0.01}_{-0.02}$	$8.96^{+0.66}_{-0.89}$	$3.32^{+0.46}_{-0.92}$	$0.05^{+0.05}_{-0.03}$

Notes.
[a] Fits to explosion energies are very close to the model grid parameter boundaries.
[b] Events with relatively less confident inferences due to poor data quality (including missing phases of the light curve along with no constraints on upper limits).

ZTF21aabygea (SN 2021os) and ZTF18abcpmwh (SN 2018cur) yielded the highest ZAMS masses ($15.96^{+0.03}_{-0.19}$ and $15.77^{+0.20}_{-1.39}$ $M_\odot$, respectively), while ZTF21aagtqpn (SN 2021bkq) has the lowest ($12.11^{+0.17}_{-0.08}$ $M_\odot$). The highest explosion energies are seen for ZTF18acuqskr (SN 2018jrb) and ZTF20aausahr (SN 2020hgm) ($2.90^{+0.30}_{-0.39} \times 10^{51}$ and $2.38^{+0.46}_{-0.38} \times 10^{51}$ erg, respectively). As shown in Figure 1, these two events correspond to steeper and early declines in the light curves as compared to low energetic events ($\sim 0.5 \times 10^{51}$ erg), including ZTF19ackjvtl (SN 2019uwd) and ZTF19acbvisk (SN 2019rms). These observed short-lived plateaus and fast declines are in agreement with previous results for other high-energy CCSNe (Valenti et al. 2016; Rubin & Gal-Yam 2017; de Jaeger et al. 2019; Barker et al. 2021). The more

energetic events in our sample also show increased peak luminosity in both the ztf-g and ztf-r bands (Sanders et al. 2015; Galbany et al. 2016; Valenti et al. 2016).

For seven events, our estimates of kinetic energy favor the minimum parameter value of our grid (0.5×10^{51} erg). We flag these events as ones for which our model fits are less confident, since the actual kinetic energy may be significantly lower.

Most events (37 out of 45) in our sample tend to favor mass-loss rates between $10^{-4.0}$ and $10^{-2.0} M_{\odot}\,\mathrm{yr}^{-1}$. However, a non-negligible number of events (eight out of 45) yield higher mass-loss rate estimates $\leqslant 10^{-2.0} M_{\odot}\,\mathrm{yr}^{-1}$. This finding is consistent with the findings of Förster et al. (2018), who reported higher mass-loss rates to be correlated with early and steep rises in the light curves of many Type II SNe from the High cadence Transient Survey (HiTS; Förster et al. 2016), possibly due to shock breakout in dense CSM (Moriya et al. 2011, 2017, 2018; Morozova et al. 2015, 2018; Bruch et al. 2021; Haynie & Piro 2021). We find that the fits for the steepness parameter β are most likely prior dominated and favor values closer to $\beta \sim 3$, consistent with slowly accelerating winds found in RSGs (Baade et al. 1996).

ZTF19abguqsi (SN 2019lsh) produced the least ^{56}Ni mass of 0.01 ± 0.01 $M_{\odot}$. Other ZTF events in the sample have estimates of ^{56}Ni mass ranging from 0.02–0.1 $M_{\odot}$. ZTF19aabvkly (SN 2019fmv), ZTF19abiahko (SN 2019lsj), and ZTF20aazcnrv (SN 2020jjj) have relatively short-lived plateau regions in their light curves and are associated with lower estimates of synthesized ^{56}Ni mass (see Figure 1). Events with higher estimates of ^{56}Ni mass have long-lived plateaus as compared to the events with lower ^{56}Ni mass estimates and faster declines in their light curves. These results are in agreement with previous analyses of SNe Type II that consider how ^{56}Ni mass affects light-curve evolution (Eastman et al. 1994; Bersten 2013; Faran et al. 2014; Kozyreva et al. 2019).

ZTF20abyosmd (SN 2020toc) has the highest host extinction ($A_V = 1.03^{+0.19}_{-0.11}$ mag), followed by ZTF21aaevrjl (SN 2021arg) ($A_V = 0.81^{+0.30}_{-0.32}$ mag). ZTF18acbwasc (SN 2018hfc) and ZTF21aabygea (SN 2021os) have negligible host extinction values (both $A_V = 0.02^{+0.02}_{-0.01}$ mag). All ZTF events in our sample show host extinction values ranging from $A_V = 0.01$–1.1 mag, typical for CCSNe hosts (Pastorello et al. 2006; Maguire et al. 2010; Faran et al. 2014).

4.1. Correlations between Physical Parameters

We plot our inferred values with a comparison to other similar works in the literature (Förster et al. 2018; Martinez et al. 2020) in Figure 2. Förster et al. (2018) use hydrodynamical models on HiTS Type II SNe that include estimates of the circumstellar environment, while Martinez et al. (2020) do not include CSM structure in their models. Figure 2 shows the bounds of our model grid with gray-dotted lines for each parameter in the plot. The ZTF events whose energy value fits approached the bounds of the model grid are marked in Table 3. We represent events that had relatively narrower prior distribution for the date of the explosion inside the purple circle in Figure 2. These events had either constraining upper limits before the first detection or enough rise-time data to make an educated guess on the upper bound of the prior distribution for the date of the explosion.

Generally, our parameter estimates are less confident for ZTF events with poor data quality, such as those missing phases of light curves combined with unavailable upper-limit constraints and whose parameter values approached the parameter boundaries of the model grid (see Table 3). These events are represented by green circles in Figure 2 as flagged events. Among seven out of 11, ZTF18acbwasc (SN 2018hfc), ZTF19abhduuo (SN 2019lre), ZTF19abqyouo (SN 2019pbk), ZTF19ackjvtl (SN 2019uwd), ZTF20abyosmd (SN 2020toc), ZTF20acjqksf (SN 2020tfb), and ZTF20acnvtxy (SN 2020zkx) can be grouped together as events that have higher values for the time of the explosion (>25 days). This could be attributed to the fact that the prior distribution was too broad as there were no upper limits for these events as provided by the ZTF survey. The remaining four ZTF events whose fits approached the model boundaries are ZTF18acbvhit (SN 2018hle), ZTF19abvbrve (SN 2019puv), ZTF20acptgfl (SN 2020zjk), and ZTF21aafkwtk (SN 2021apg).

Moreover, we performed a Pearson correlation analysis to check if we can find any correlations between the physical parameters. However, we were unable to find any significant correlations ($r > +0.5$ or $r < -0.5$) within the sample studied. The correlation matrix is shown in Figure 3. The modest mass range in our model grid (12–16 $M_{\odot}$) limits our ability to make strong claims on any potential ZAMS dependencies. For example, in Figure 2, the correlations in Martinez et al. (2020) only become clear when the ZAMS range is extended to 10 $M_{\odot}$. Our hydrodynamical grid explores new parameter spaces that include mass-loss properties and this can possibly introduce additional degeneracies.

5. Real-time Parameter Evolution

We analyzed how each of the parameter fits evolved as a function of time, termed *real-time characterization*. We were motivated to characterize how well or poorly the model parameter fits and their uncertainties at fractional light-curve stages anticipated the values found from complete light curves. We compared our model grid to three regimes of incomplete light curves with respect to the first detection: (1) $\Delta t \leqslant 25$ days, (2) $\Delta t \leqslant 50$ days, and (3) all available data.

Figure 4 shows a detailed evolving characterization for the event ZTF19aaqdkrm (SN 2019dod). As expected, the fits and estimates of the parameters change with time as the SN evolves and additional measurements are incorporated into the fitting process. Within $\Delta t \leqslant 25$ days and $\Delta t \leqslant 50$ days, the fits favor lower ^{56}Ni masses and higher energies. As data in both bands accumulate, the fits favor higher ^{56}Ni masses and lower energies. At $\Delta t \geqslant 50$ days, the portion of the light curve powered by hydrogen recombination of the event starts to fall off, giving better estimates on ZAMS and ^{56}Ni masses.

We performed this same analysis on all 45 ZTF events, where similar trends are seen. Figure 5 shows the difference in parameter values of our fits with respect to the final epoch with all the data as the event unfolds. Our analysis shows that the explosion energies and mass-loss rates for the events are initially overestimated and tend to favor lower final values when all data is included in the fit. This is opposite to what we see in the case of ^{56}Ni mass, as it is underestimated with only a few measurements and consistently favors higher values for many events during later stages of light-curve evolution as the recombination drop-off starts to unfold.

The most confident estimate of ^{56}Ni mass is inferred when the hydrogen recombination phase ends and the radioactive decay phase starts. This results in epochs with all the data yielding higher estimates of ^{56}Ni mass. With kinetic energy, the

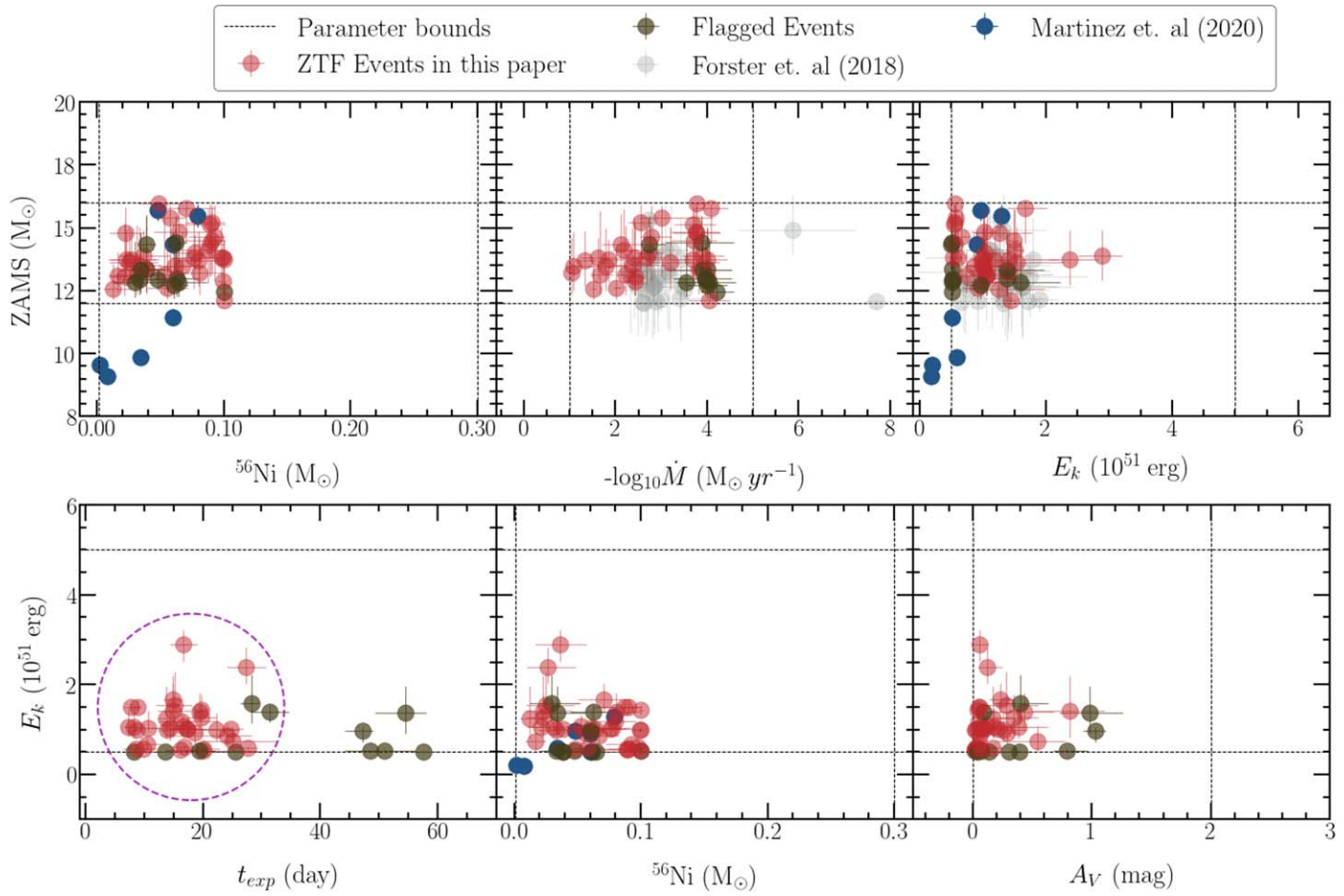

Figure 2. Top panel: ZAMS mass plotted against ^{56}Ni mass, mass-loss rate, and kinetic energy. The blue and gray circles denote the values that were found for SNe II in Förster et al. (2018) and Martinez et al. (2020). Bottom panel: kinetic energy plotted against the time of the explosion with respect to the first detection, ^{56}Ni mass, and host extinction (A_V). The gray-dotted lines represent the parameter bounds of our model grid. The purple circle in the bottom left panel demarcates events that required a narrower prior distribution for the date of the explosion constrained either from upper limits or rise-time data. The green circles represent flagged ZTF events with low-confidence model fits.

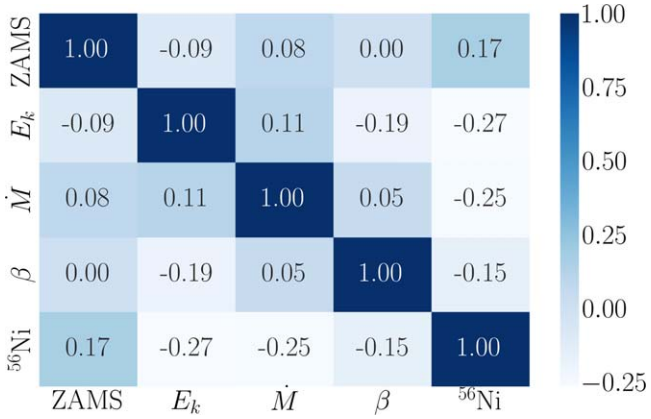

Figure 3. Pearson correlation matrix showing correlation coefficients that are color coded for different physical parameters in the analysis. No significant correlations between physical parameters were found within the sample of the Type II SNe used in this study.

peak luminosity and decline rate of the light curve play a significant role in estimating the energetics of the event. As a result, as more data become available at later epochs, more reliable estimates of kinetic energy will be seen. The inferred values of ZAMS, host extinction, date of the explosion, and the β remain nearly constant as the light curve evolves.

6. Discussion

6.1. Parameter Space Degeneracy

A major challenge encountered when modeling only two passbands provided by public ZTF light curves was model degeneracy. Specifically, the probability that different combinations of explosion and progenitor parameters can potentially lead to the same light curve posed difficulties in converging to a unique solution in our fitting method. As noted in previous works, the hydrodynamical modeling approach has led to larger estimates of progenitor properties, especially ZAMS estimates, when compared to other approaches like pre-SN explosion imaging (Utrobin & Chugai 2008, 2009; Maguire et al. 2010; Sanders et al. 2015). In the Appendix, the posterior distribution of three ZTF events at various epochs is examined using kernel density estimation (KDE) analysis, along with a calculation of the number of modes. In a similar analysis for all 45 events, we find that all the ZTF events have multimodal posteriors and the temporal evolution of modes cannot be generalized.

Goldberg et al. (2019) recognize the challenges involved in breaking the degeneracies between ejecta mass, explosion energy, and progenitor radius, and argue that in order to do so requires an independent measurement of one of the parameters. The scaling relationships used in their work yield families of explosions with varied parameters that can reproduce similar light curves. Hillier

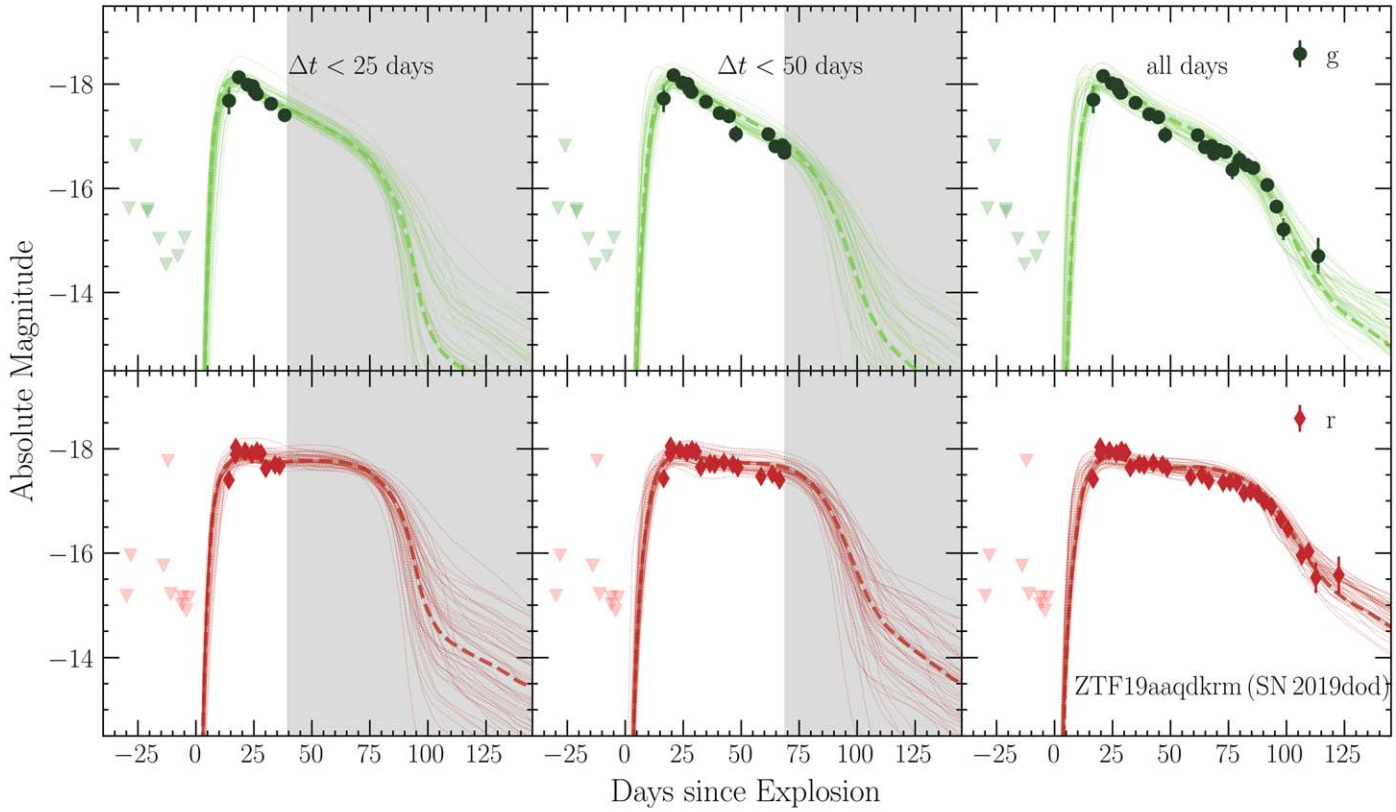

	$\Delta t < 25$ days	$\Delta t < 50$ days	all days
ZAMS ($M_\odot$)	$13.37^{+1.40}_{-0.92}$	$13.09^{+1.84}_{-0.76}$	$13.14^{+2.52}_{-0.81}$
E_k (10^{51} erg)	$1.44^{+0.28}_{-0.24}$	$1.19^{+0.29}_{-0.31}$	$1.08^{+0.25}_{-0.28}$
-$\log_{10} \dot{M}$ ($M_\odot\, yr^{-1}$)	$1.94^{+0.22}_{-0.22}$	$1.70^{+0.25}_{-0.11}$	$1.67^{+0.25}_{-0.21}$
β	$3.02^{+0.85}_{-0.85}$	$3.00^{+0.91}_{-0.97}$	$3.06^{+0.89}_{-1.20}$
^{56}Ni ($M_\odot$)	$0.03^{+0.02}_{-0.02}$	$0.02^{+0.02}_{-0.01}$	$0.05^{+0.02}_{-0.01}$
t_{exp} (day)	$14.19^{+2.94}_{-2.21}$	$16.58^{+2.16}_{-3.13}$	$16.68^{+1.95}_{-2.88}$
A_V (mag)	$0.10^{+0.12}_{-0.07}$	$0.14^{+0.15}_{-0.10}$	$0.12^{+0.11}_{-0.08}$

Figure 4. Multi-epoch real-time characterization for ZTF19aaqdkrm (SN 2019dod). The left panel shows the model fits to only data within the first 25 days of detection in each individual band. The middle panel shows model fits using data within the first 50 days of detection. The right panel uses all data. The light curves are plotted with respect to the derived time of the explosion and host extinction from model fits at each epoch. The table below shows parameter estimates derived from fits at each epoch.

& Dessart (2019) also highlight calculations of similar photospheric phases for well-sampled Type II SNe in their multi-band and spectroscopic modeling.

Martinez et al. (2020) attempt to partially lift this degeneracy issue by fitting photospheric velocity information from their models to velocity measurements obtained of SNe during the plateau phase. However, Goldberg et al. (2019) argue that only the ejecta velocities measured during the initial shock cooling phase can be useful to break these degeneracies seen in the parameters. Our analysis focused on photometry only, and future work can investigate whether the use of kinematic information from spectroscopy can better constrain parameter selection.

6.2. Bolometric versus Precomputed Multi-band Inference

Our analysis adopts the approach of fitting observations to synthetic multi-band photometry derived from theoretical hydrodynamical models. Similar works like Nicholl et al. (2017) and Guillochon et al. (2018) use semi-analytical, blackbody SED models to fit multi-band photometry for transients. These procedures contrast with typical methods that first construct bolometric light curves from multi-filter and/or multiwavelength observations, which are in turn compared to model bolometric light curves. Each method has associated uncertainties. In the case of synthetic model photometry, uncertainties arise from assumptions in opacity treatment at different frequencies in STELLA. In the case of creating bolometric light curves from interpolated observed data sets, the uncertainties stem from potential gaps in photometry cadence, limited passbands, and potentially few data points overall to fit against.

For real-time characterization of events, we found that a proper Bayesian inference of explosion parameters for large

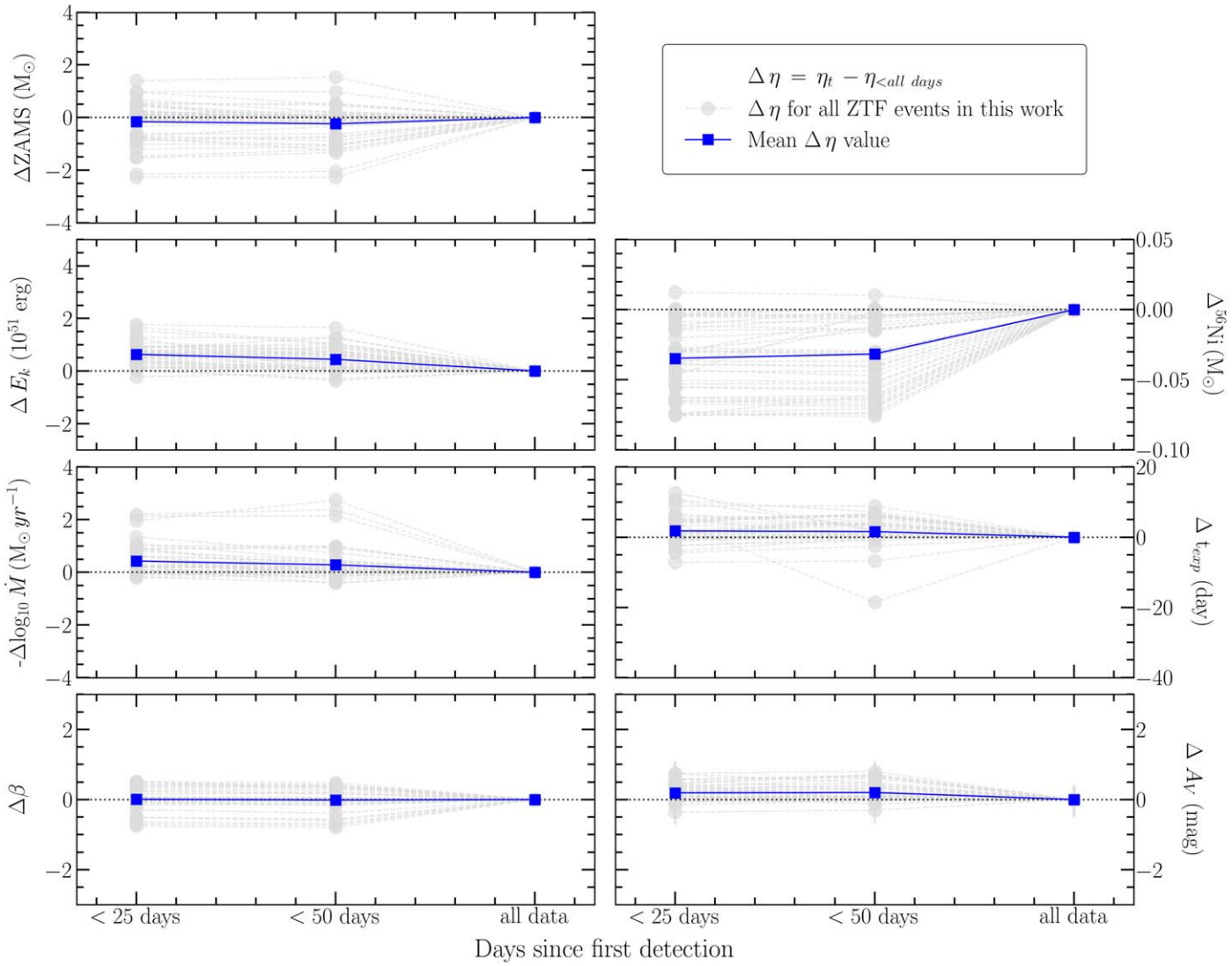

Figure 5. Real-time parameter evolution for all the listed ZTF events. The average change in parameter values (averaged over all 45 ZTF events) at each epoch with respect to the final epoch with all data are represented by the blue squares from top left to bottom right. The order of the parameters are as follows: ZAMS mass, the kinetic energy of the explosion (E_k), mass-loss rate ($\dot{M}$), steepness of velocity law (β) associated with the stellar wind and ^{56}Ni mass synthesized, the date of the explosion with respect to the first detection, and host extinction (A_V).

numbers of SNe is most efficiently conducted with precomputed grids of models. Computing models in real time per event will lead to duplicative efforts and incur computational time costs. With our method, the fitting is more rapid, more flexible, and the associated uncertainties are less significant.

6.3. Intelligent Augmentation

Our analysis only uses ZTF public data in the ztf-*g* and ztf-*r* passbands to make inferences about Type II explosion parameters. Our parameter fits could be further constrained with observations at other passbands, and it is worthwhile to consider *which passbands* at *which epochs* are most constraining. To this end, inferring transients in real time in order to make on-the-fly decisions about optimal follow-up in complementary passbands is needed (Carbone & Corsi 2020; Sravan et al. 2021). Generally, most constraining for inferring Type II properties are observations at early and late phases of light-curve evolution. At early phases, UV observations best sample shock-breakout and circumstellar interaction (Gezari et al. 2015; Ganot et al. 2016; Soumagnac et al. 2020; Haynie & Piro 2021; Jacobson-Galán et al. 2022). At late phases, near- and mid-infrared passbands provide diagnostics that best follow ejecta cooling and dust formation (Szalai & Vinkó 2013; Bianco et al. 2014; Tinyanont et al. 2016). Optimally augmenting all-sky survey photometry in real time in this way can enhance opportunities to generate large samples of CCSNe sufficiently observed to perform population and host-environment studies (D'Andrea et al. 2010; Anderson et al. 2014; Sanders et al. 2015; Schulze et al. 2021).

6.4. Anomaly Detection

Our work uncovered two examples of anomalous Type II SNe, which are not included in our sample of 45 events. We present the unusual light curves of ZTF18acgvgiq (SN 2018fru) and ZTF20acwxrgp (SN 2020acjg) in Figure 6. The fits for the entire light curves converged to a model solution with very poor likelihood scores resulting in inaccurate inferences. Consequently, we were unable to characterize these events with our current model grid. The anomalous nature of these events could be identified via poor model fits as early as

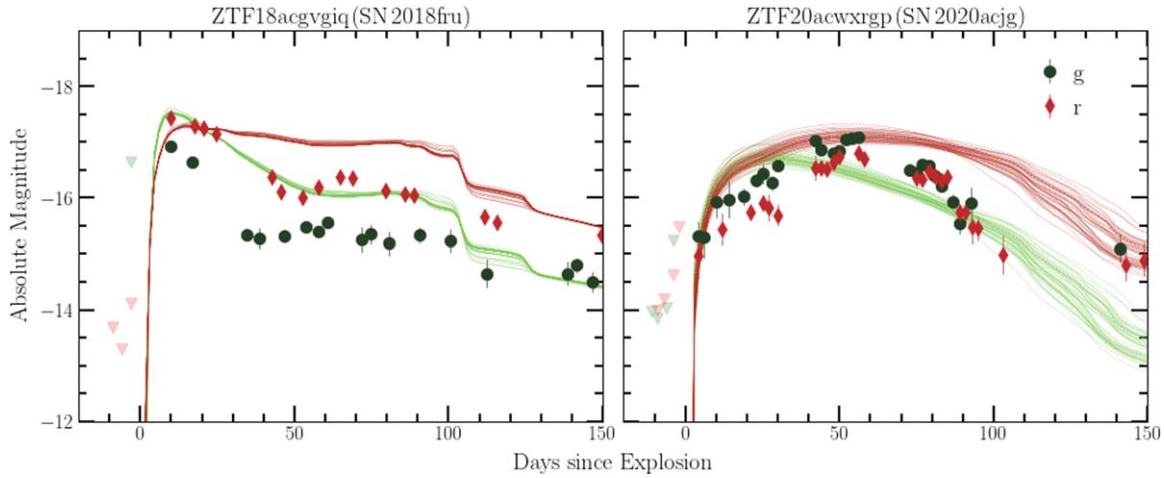

Figure 6. Spectroscopically classified Type II SNe with anomalous light curves identified in this work. Only the upper limits prior to the first detection used for deriving the fits are plotted.

$\Delta t < 25$ days. The cumulative log-evidence ($\log Z$) inferred for these two events was above -200, indicating very poor likelihood estimates when comparing the models with the data. For the events with good fits, the $\log Z$ estimates were under -20. These high $\log Z$ values indicate that the models were unable to converge to a target distribution of the parameters for the two anomalous events.

This experience shows that real-time inference can be used as a way to identify targets that deviate from normal theoretical predictions. Such real-time analyses for detecting anomalies (Pruzhinskaya et al. 2019; Soraisam et al. 2020; Villar et al. 2020, 2021; Ishida et al. 2021; Martínez-Galarza et al. 2021) can be automated into an ORACLE such as REFITT to motivate rapid spectroscopic follow-up of nontraditional CCSNe.

7. Conclusions

In this paper, we have characterized 45 Type II SNe using only products from the public ZTF survey (i.e., in the ztf-*g* and ztf-*r* passbands) using a grid of theoretical hydrodynamical models. Our grid parameters span multiple SN progenitor and explosion properties, as well as the time of explosion with respect to the first detection and host extinction. We compare results between complete and fractional light curves to determine which parameters are most robust to incomplete photometric data sets. This effort is to assess whether opportunities exist for theoretically driven forecasts to inform when follow-up observations are needed to support all-sky survey alert streams. The following conclusions are made:

1. We obtain confident characterizations for 34 SNe II in our sample. Inferences of the remaining 11 events are limited either by poorly constraining data or the boundaries of our model grid. The properties of these well-fitted events broadly follow those reported in previous analyses of SNe II.
2. In cases where fitted parameters derived from complete versus incomplete data sets are compared, some parameters are more reliably determined at early epochs than others. The explosion energy, host extinction, and mass-loss rate parameters are overestimated during the initial phases of evolution, while the ^{56}Ni mass is underestimated. The ZAMS mass and β estimates do not change significantly at different phases.
3. The date of the explosion is a very sensitive parameter that requires well-constrained pre-explosion upper limits from the survey for confident inferences. Generally, we found parameter estimates to be less reliable for ZTF events with poor data quality, such as missing phases of the light curve along with poor upper-limit constraints.
4. Real-time Bayesian inference of progenitor and explosion parameters for large numbers of CCSNe from all-sky surveys demand a precomputed grid of models. Creating synthetic model light curves in respective all-sky survey passbands catalyzes real-time characterization of evolving transients by avoiding the challenges associated with constructing bolometric light curves with sparse and incomplete photometry.

Our work has demonstrated that hydrodynamical model grids for CCSNe along with statistical analyses can provide opportunities to enhance the scientific return from all-sky surveys that provide live alert streams. Theoretically driven predictions can be leveraged to efficiently coordinate world-wide observing facilities to conduct follow-up observations that augment survey light curves to optimally achieve scientific objectives (Bianco et al. 2014; Modjaz et al. 2019; Kennamer et al. 2020; Sravan et al. 2020; Anand et al. 2021).

For example, real-time characterization can identify and prioritize transients that fall within certain parameter spaces of interest, including the extreme high and low ends of kinetic energy or ^{56}Ni mass. Likewise, theoretical forecasts can identify and prioritize follow-up photometry at critical phases of transient evolution, including monitoring the plateau drop-off of SNe II light curves that provides information needed to improve estimates of kinetic energy and ZAMS and ^{56}Ni masses. Ideally, predicting transient evolution using the underlying physics of transients can be incorporated into a TOM or ORACLE that can efficiently recommend targets for follow-up at information-rich epochs (Djorgovski et al. 2016; Street et al. 2018; Kasliwal et al. 2019; Sravan et al. 2020; Agayeva et al. 2021).

Our future work relies on an expanded grid of hydrodynamical models exploring larger parameter ranges, including varying degrees of ^{56}Ni mixing within the inner layers of the

progenitors, and information on photospheric velocity that can be used to potentially break degeneracies between parameters. It will also expand synthetic photometry to all six passbands of LSST. Although our work focuses on Type II CCSNe, our methods can be easily applied to identify, prioritize, and coordinate follow-up of other transients discovered by the Vera C. Rubin Observatory.

The authors would like to thank the anonymous referee for helpful comments that have significantly improved this paper. We also acknowledge helpful discussions with Thomas Matheson, Mariana Orellana, and Melina Bersten. The ZTF forced-photometry service was funded under the Heising-Simons Foundation grant #12540303 (PI: Graham). Numerical computations were in part carried out on a PC cluster at the Center for Computational Astrophysics (CfCA), National Astronomical Observatory of Japan. D.M. acknowledges NSF support from grants PHY-1914448, PHY-2209451, AST-2037297, and AST-2206532.

Software: KEPLER (Weaver et al. 1978), STELLA (Blinnikov et al. 1998, 2000, 2006; Moriya et al. 2017, 2018; Ricks & Dwarkadas 2019), astropy (Astropy Collaboration et al. 2013, 2018), dynesty (Skilling 2004).

Appendix
Multi-epoch Evolution of Posterior Distribution of Parameters

We show the light curve model fits for the remaining events in our samples in Figures 7 and 8, which are extented versions of Figure 1. Figures 9 and 10 shows the multi-epoch real-time characterization for the events ZTF20abwdaeo (SN 2020rvn) and ZTF21aabygea (SN 2021os). Figures 11–13 shows the corner plots with posterior probability distribution for various

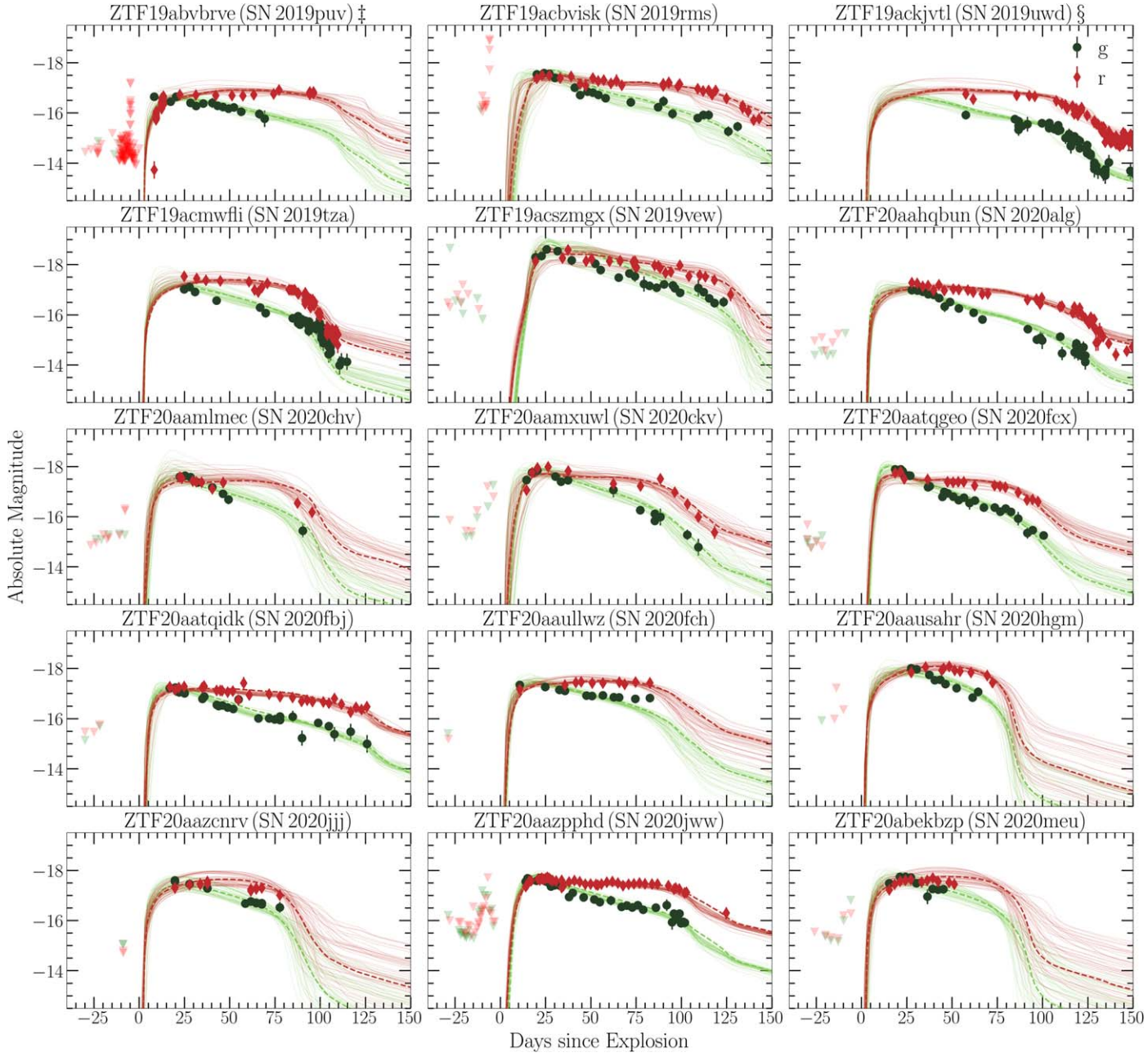

Figure 7. Continued from Figure 1.

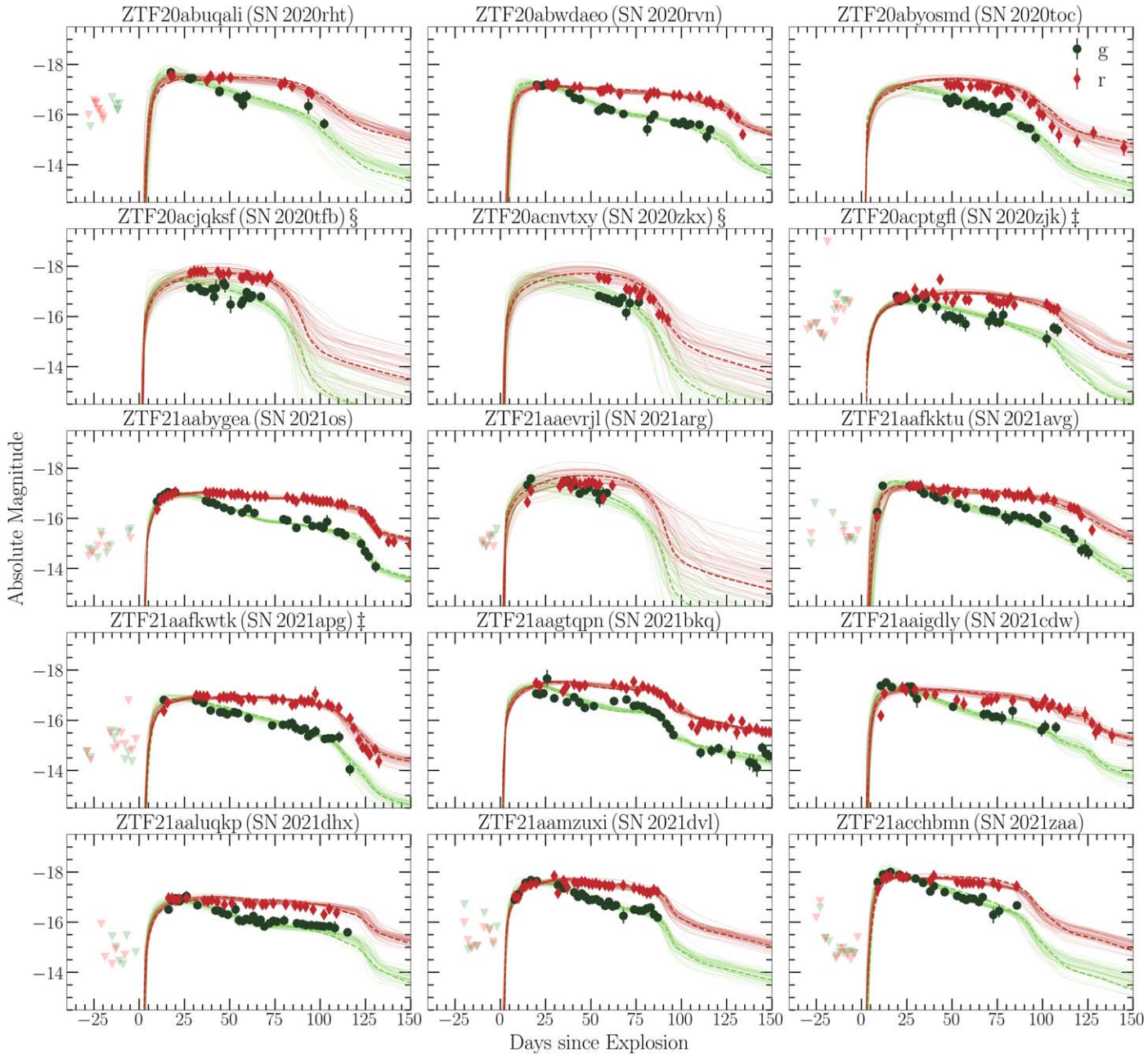

Figure 8. Continued from Figure 1.

physical parameters for ZTF20acptgfl (SN 2020zjk), ZTF20aausahr (SN 2020hgm) and t ZTF19abqyouo (SN 2019pbk), respectively.

We performed a KDE analysis in order to find the modality of the posterior distributions at various epochs. The samples in the posterior distribution were collected and smoothed using Silverman's bandwidth with a Gaussian kernel. The KDE approximated distribution was then used to calculate the number of modes at every epoch. The modes were found by identifying inflection points in the distribution, i.e., positions where the first derivative changes sign.

We found that all the objects have multimodal posteriors for at least one parameter in our analysis. From this analysis, we conclude that the change in the posteriors for physical parameters over different epochs cannot be generalized for all the events. Figure 14 shows examples of multimodal posteriors for ZAMS, kinetic energy, and ^{56}Ni for three ZTF events The red circles represent the different modes found in the distribution using inflection point analysis. We note that the modes of the distribution for kinetic energy shift from higher to lower values as time proceeds as shown in Figure 14 for each event as discussed in this paper. The trend in ^{56}Ni with time is reflected in the modes with earlier epochs favoring lower values as compared with final epochs. The degeneracies in parameter space as discussed in Section 6.1 are clearly reflected in these distributions through multi-modality.

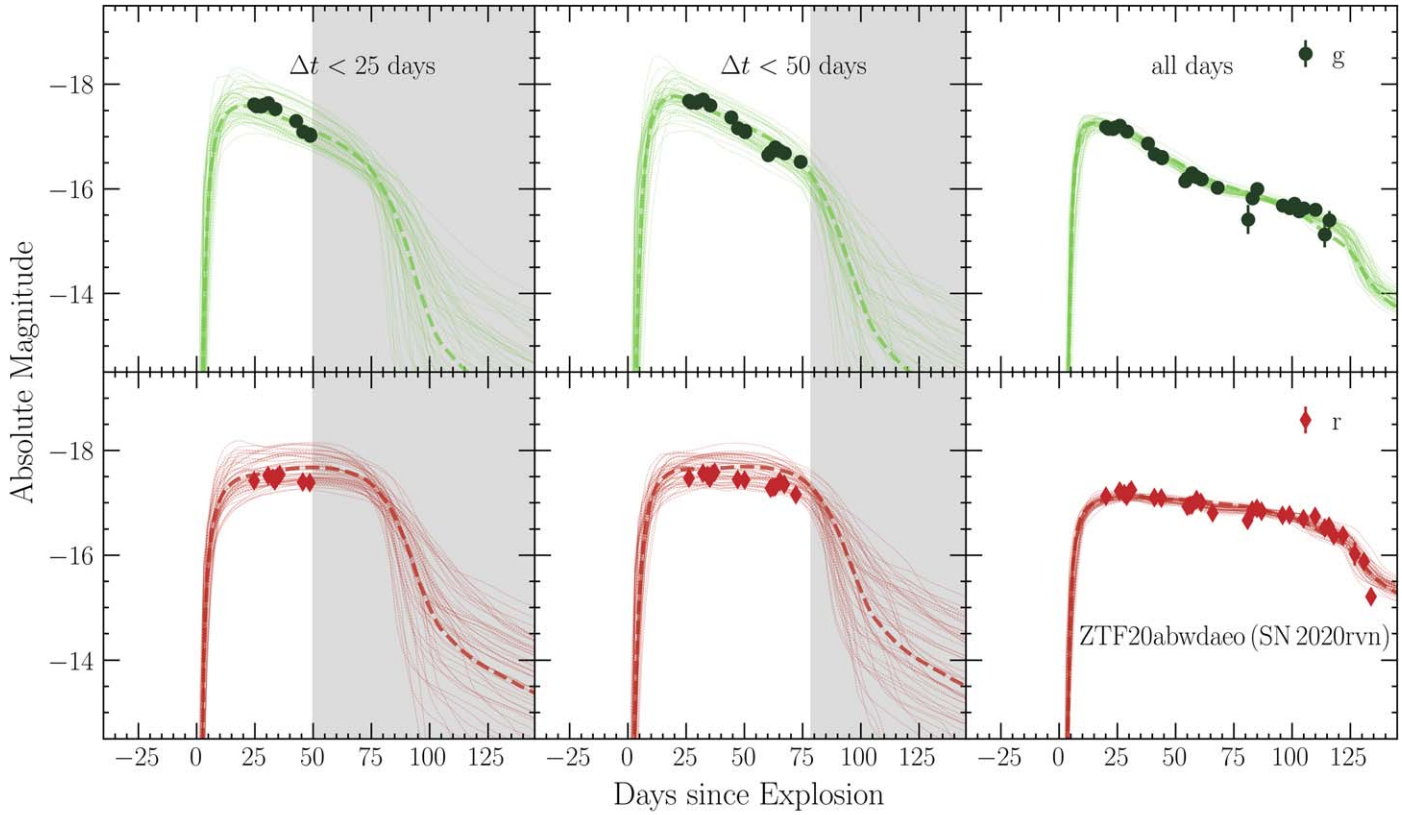

	$\Delta t < 25$ days	$\Delta t < 50$ days	all days
ZAMS ($M_\odot$)	$13.74^{+1.38}_{-1.14}$	$13.99^{+1.73}_{-1.36}$	$15.22^{+0.71}_{-1.95}$
E_k (10^{51} erg)	$1.24^{+0.83}_{-0.46}$	$1.20^{+0.70}_{-0.51}$	$0.57^{+0.03}_{-0.03}$
-$\log_{10} \dot{M}$ ($M_\odot\, yr^{-1}$)	$2.77^{+1.24}_{-0.59}$	$2.28^{+1.31}_{-0.45}$	$2.55^{+0.26}_{-0.27}$
β	$2.99^{+0.56}_{-0.51}$	$2.90^{+0.69}_{-0.48}$	$3.50^{+0.28}_{-1.08}$
^{56}Ni ($M_\odot$)	$0.02^{+0.02}_{-0.02}$	$0.03^{+0.02}_{-0.02}$	$0.09^{+0.01}_{-0.02}$
t_{exp} (day)	$24.68^{+4.46}_{-3.83}$	$26.27^{+4.26}_{-3.45}$	$20.09^{+2.75}_{-2.49}$
A_V (mag)	$0.43^{+0.31}_{-0.24}$	$0.50^{+0.26}_{-0.25}$	$0.03^{+0.03}_{-0.02}$

Figure 9. Continued from Figure 4 for the event ZTF20abwdaeo (SN 2020rvn).

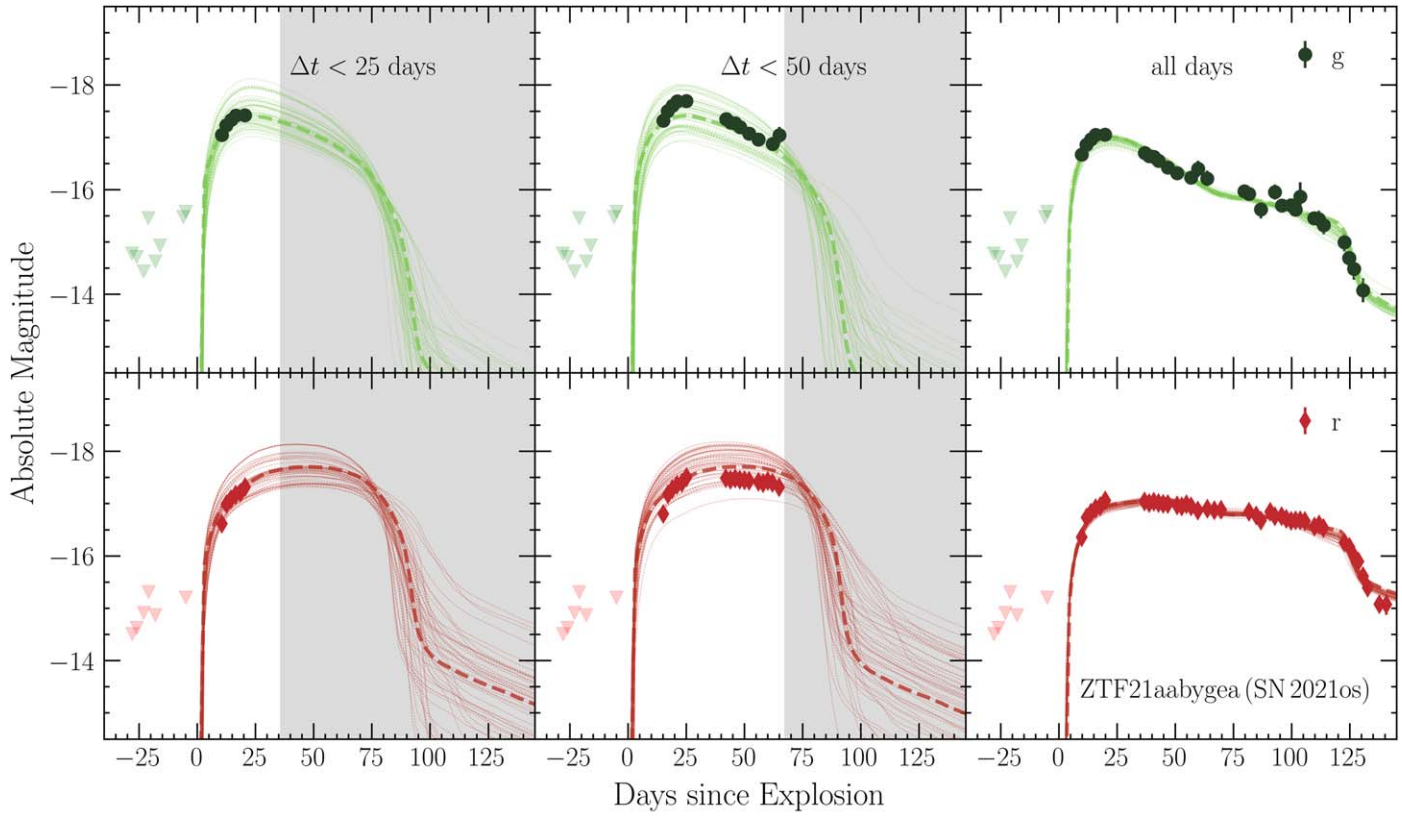

	$\Delta t < 25$ days	$\Delta t < 50$ days	all days
ZAMS ($M_\odot$)	$13.70^{+1.22}_{-1.12}$	$13.69^{+1.34}_{-1.08}$	$15.96^{+0.03}_{-0.19}$
E_k (10^{51} erg)	$1.47^{+0.69}_{-0.52}$	$1.52^{+0.69}_{-0.58}$	$0.57^{+0.02}_{-0.02}$
-$\log_{10}\dot{M}$ ($M_\odot\, yr^{-1}$)	$4.01^{+0.18}_{-0.19}$	$3.98^{+0.22}_{-0.20}$	$3.76^{+0.18}_{-0.14}$
β	$3.00^{+0.49}_{-0.49}$	$2.95^{+0.55}_{-0.51}$	$3.75^{+0.05}_{-0.05}$
^{56}Ni ($M_\odot$)	$0.02^{+0.02}_{-0.01}$	$0.02^{+0.02}_{-0.01}$	$0.05^{+0.02}_{-0.02}$
t_{exp} (day)	$10.52^{+3.93}_{-2.75}$	$15.07^{+2.27}_{-2.17}$	$9.84^{+0.87}_{-0.98}$
A_V (mag)	$0.37^{+0.31}_{-0.24}$	$0.62^{+0.26}_{-0.29}$	$0.02^{+0.02}_{-0.01}$

Figure 10. Continued from Figure 4 for the event ZTF21aabygea (SN 2021os).

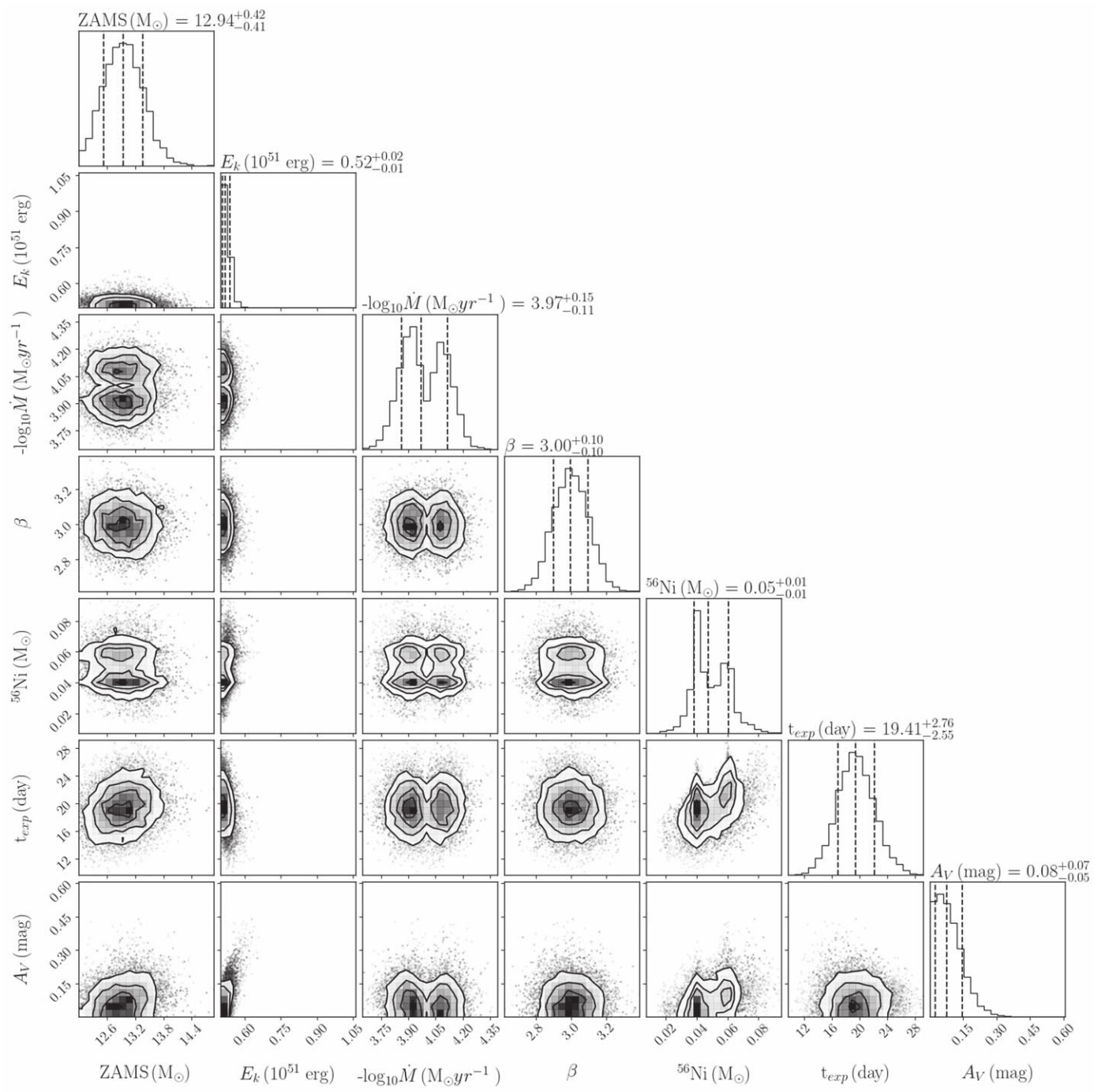

Figure 11. Corner plot showing the posterior probability distribution of various parameters for the event ZTF20acptgfl (SN 2020zjk).

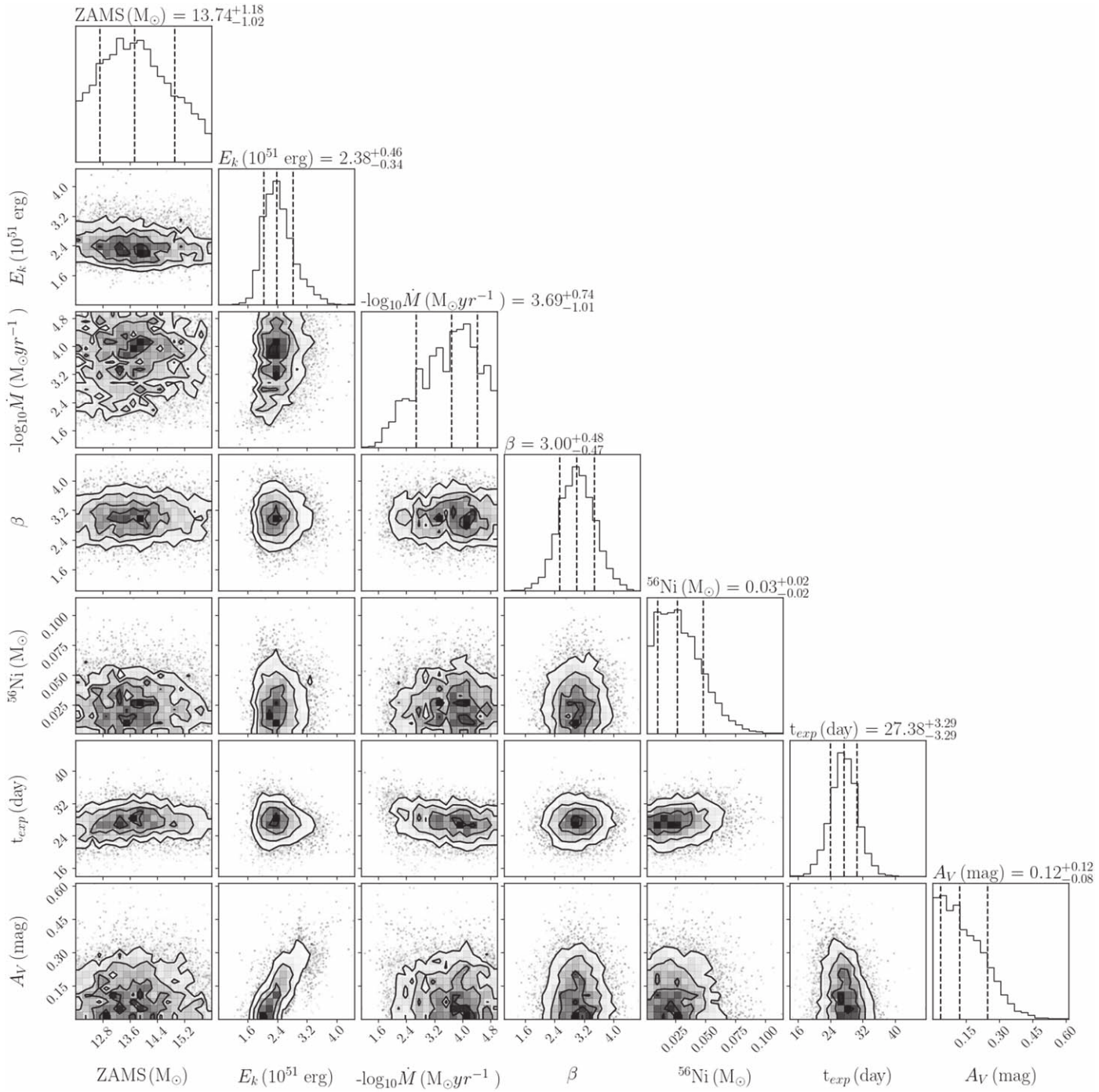

Figure 12. Corner plot showing the posterior probability distribution of various parameters for the event ZTF20aausahr (SN 2020hgm).

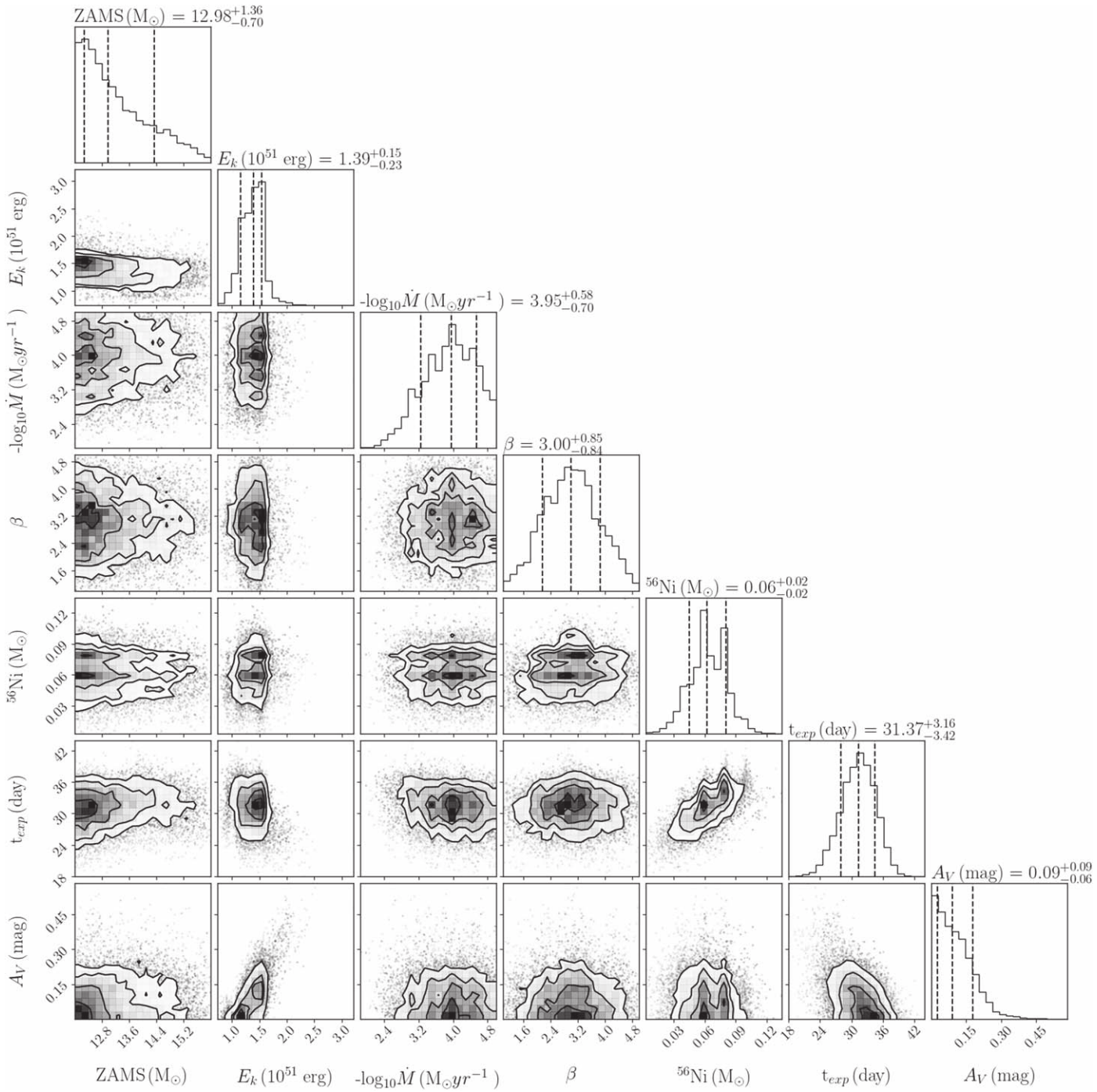

Figure 13. Corner plot showing the posterior probability distribution of various parameters for the event ZTF19abqyouo (SN 2019pbk).

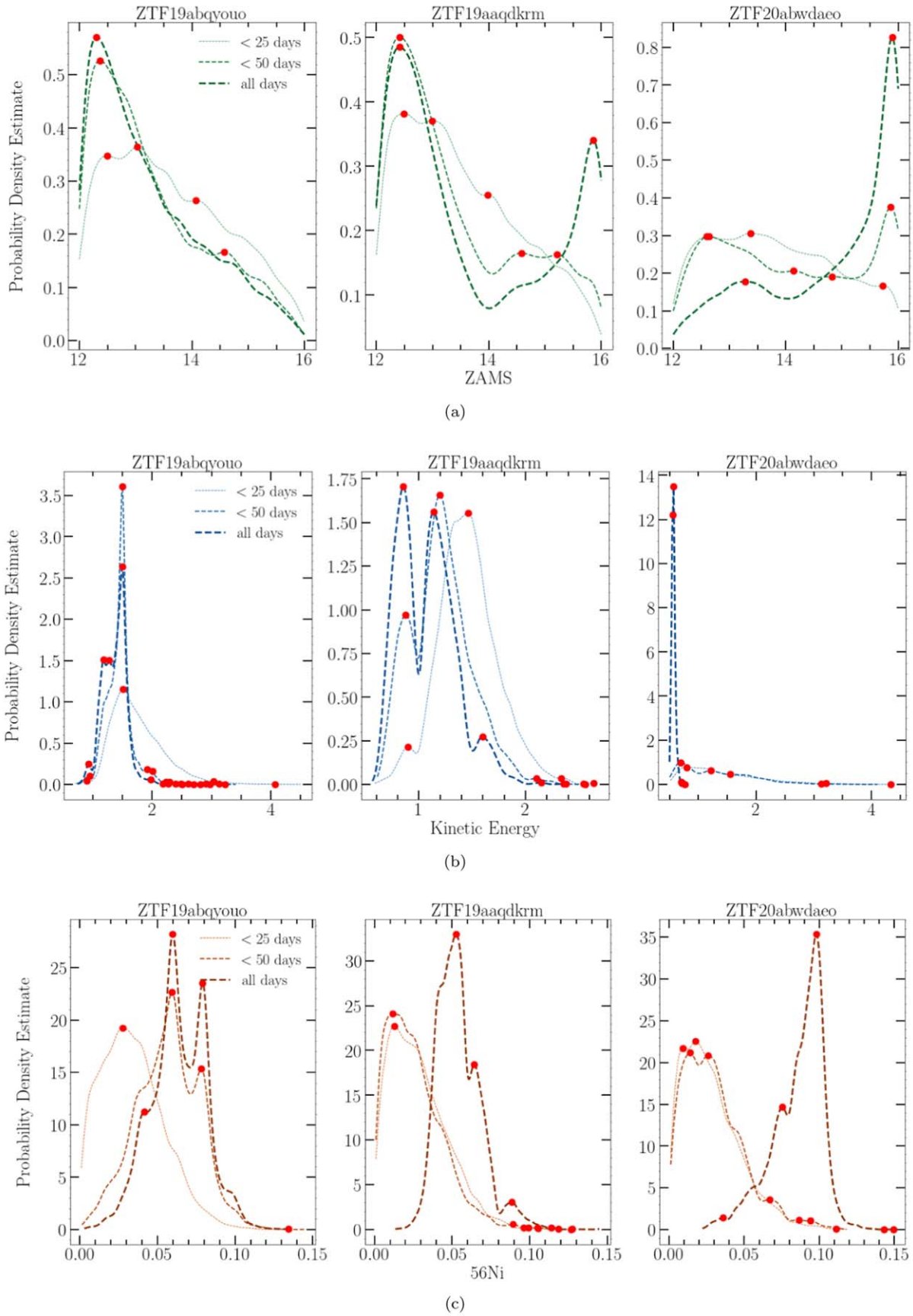

Figure 14. KDE of physical parameters along with modes represented by red circles obtained at three epochs for three ZTF events. The order of physical parameters from top to bottom row are as follows: (a) ZAMS mass, (b) kinetic energy, and (c) ^{56}Ni mass.

ORCID iDs

Bhagya M. Subrayan https://orcid.org/0000-0001-8073-8731
Dan Milisavljevic https://orcid.org/0000-0002-0763-3885
Takashi J. Moriya https://orcid.org/0000-0003-1169-1954
Kathryn E. Weil https://orcid.org/0000-0002-8360-0831
Geoffery Lentner https://orcid.org/0000-0001-9314-0683
John Banovetz https://orcid.org/0000-0003-0776-8859
Braden Garretson https://orcid.org/0000-0001-6922-8319
Jack Reynolds https://orcid.org/0000-0002-1521-0479
Ryan Chornock https://orcid.org/0000-0002-7706-5668
Raffaella Margutti https://orcid.org/0000-0003-4768-7586

References

Agayeva, S., Alishov, S., Antier, S., et al. 2021, RMxAC, 53, 198
Alves, C. S., Peiris, H. V., Lochner, M., et al. 2022, ApJS, 258, 23
Anand, S., Coughlin, M. W., Kasliwal, M. M., et al. 2021, NatAs, 5, 46
Anderson, J. P., González-Gaitán, S., Hamuy, M., et al. 2014, ApJ, 786, 67
Astropy Collaboration, Price-Whelan, A. M., Sipőcz, B. M., et al. 2018, AJ, 156, 123
Astropy Collaboration, Robitaille, T. P., Tollerud, E. J., et al. 2013, A&A, 558, A33
Baade, R., Kirsch, T., Reimers, D., et al. 1996, ApJ, 466, 979
Barker, B. L., Harris, C. E., & Warren, M. L. 2021, ApJ, 934, 67
Bellm, E. C., Kulkarni, S. R., Graham, M. J., et al. 2019, PASP, 131, 018002
Bersten, M. C. 2013, arXiv:1303.0639
Bianco, F. B., Modjaz, M., Hicken, M., et al. 2014, ApJS, 213, 19
Blinnikov, S., Lundqvist, P., Bartunov, O., Nomoto, K., & Iwamoto, K. 2000, ApJ, 532, 1132
Blinnikov, S. I., Eastman, R., Bartunov, O. S., Popolitov, V. A., & Woosley, S. E. 1998, ApJ, 496, 454
Blinnikov, S. I., Röpke, F. K., Sorokina, E. I., et al. 2006, A&A, 453, 229
Borne, K. D. 2008, AN, 329, 255
Bruch, R. J., Gal-Yam, A., Schulze, S., et al. 2021, ApJ, 912, 46
Carbone, D., & Corsi, A. 2020, ApJ, 889, 36
D'Andrea, C. B., Sako, M., Dilday, B., et al. 2010, ApJ, 708, 661
de Jaeger, T., Zheng, W., Stahl, B. E., et al. 2019, MNRAS, 490, 2799
Djorgovski, S. G., Graham, M. J., Donalek, C., et al. 2016, arXiv:1601.04385
Eastman, R. G., Woosley, S. E., Weaver, T. A., & Pinto, P. A. 1994, ApJ, 430, 300
Faran, T., Poznanski, D., Filippenko, A. V., et al. 2014, MNRAS, 442, 844
Förster, F., Cabrera-Vives, G., Castillo-Navarrete, E., et al. 2021, AJ, 161, 242
Förster, F., Maureira, J. C., San Martín, J., et al. 2016, ApJ, 832, 155
Förster, F., Moriya, T. J., Maureira, J. C., et al. 2018, NatAs, 2, 808
Galbany, L., Hamuy, M., Phillips, M. M., et al. 2016, AJ, 151, 33
Ganot, N., Gal-Yam, A., Ofek, E., et al. 2016, ApJ, 820, 57
García-Jara, G., Protopapas, P., & Estévez, P. A. 2022, ApJ, 935, 23
Garretson, B., Milisavljevic, D., Reynolds, J., et al. 2021, RNAAS, 5, 283
Gezari, S., Jones, D. O., Sanders, N. E., et al. 2015, ApJ, 804, 28
Goldberg, J. A., Bildsten, L., & Paxton, B. 2019, ApJ, 879, 3
Guillochon, J., Nicholl, M., Villar, V. A., et al. 2018, ApJS, 236, 6
Haynie, A., & Piro, A. L. 2021, ApJ, 910, 128
Hillier, D. J., & Dessart, L. 2019, A&A, 631, A8
Huerta, E. A., Allen, G., Andreoni, I., et al. 2019, NatRP, 1, 600
IRSA 2022, Zwicky Transient Facility Image Service, IPAC, doi:10.26131/IRSA539)
Ishida, E. E. O., Kornilov, M. V., Malanchev, K. L., et al. 2021, A&A, 650, A195
Jacobson-Galán, W. V., Dessart, L., Jones, D. O., et al. 2022, ApJ, 924, 15
Ivezić, Ž., Kahn, S. M., Tyson, J. A., et al. 2019, ApJ, 873, 111
Kasen, D., & Woosley, S. E. 2009, ApJ, 703, 2205
Kasliwal, M. M., Cannella, C., Bagdasaryan, A., et al. 2019, PASP, 131, 038003
Kennamer, N., Ishida, E. E. O., Gonzalez-Gaitan, S., et al. 2020, arXiv:2010.05941
Kochanek, C. S., Khan, R., & Dai, X. 2012, ApJ, 759, 20
Kozyreva, A., Nakar, E., & Waldman, R. 2019, MNRAS, 483, 1211
LSST Science Collaboration, Abell, P. A., Allison, J., et al. 2009, arXiv:0912.0201
LSST Science Collaboration, Marshall, P., Anguita, T., et al. 2017, arXiv:1708.04058
Maguire, K., Di Carlo, E., Smartt, S. J., et al. 2010, MNRAS, 404, 981
Martinez, L., Bersten, M. C., Anderson, J. P., et al. 2020, A&A, 642, A143
Martínez-Galarza, J. R., Bianco, F. B., Crake, D., et al. 2021, MNRAS, 508, 5734
Masci, F. J., Laher, R. R., Rusholme, B., et al. 2019, PASP, 131, 018003
Matheson, T., Stubens, C., Wolf, N., et al. 2021, AJ, 161, 107
Mattila, S., Dahlen, T., Efstathiou, A., et al. 2012, ApJ, 756, 111
Mauron, N., & Josselin, E. 2011, A&A, 526, A156
Modjaz, M., Gutiérrez, C. P., & Arcavi, I. 2019, NatAs, 3, 717
Möller, A., & de Boissière, T. 2020, MNRAS, 491, 4277
Möller, A., Peloton, J., Ishida, E. E. O., et al. 2021, MNRAS, 501, 3272
Moriya, T., Tominaga, N., Blinnikov, S. I., Baklanov, P. V., & Sorokina, E. I. 2011, MNRAS, 415, 199
Moriya, T. J., Förster, F., Yoon, S.-C., Gräfener, G., & Blinnikov, S. I. 2018, MNRAS, 476, 2840
Moriya, T. J., Yoon, S.-C., Gräfener, G., & Blinnikov, S. I. 2017, MNRAS, 469, L108
Morozova, V., Piro, A. L., Renzo, M., et al. 2015, ApJ, 814, 63
Morozova, V., Piro, A. L., & Valenti, S. 2018, ApJ, 858, 15
Najita, J., Willman, B., Finkbeiner, D. P., et al. 2016, arXiv:1610.01661
Narayan, G., Zaidi, T., Soraisam, M. D., et al. 2018, ApJS, 236, 9
Nicholl, M., Guillochon, J., & Berger, E. 2017, ApJ, 850, 55
Pastorello, A., Sauer, D., Taubenberger, S., et al. 2006, MNRAS, 370, 1752
Pruzhinskaya, M. V., Malanchev, K. L., Kornilov, M. V., et al. 2019, MNRAS, 489, 3591
Ricks, W., & Dwarkadas, V. V. 2019, arXiv:1906.07311
Rubin, A., & Gal-Yam, A. 2017, ApJ, 848, 8
Sánchez-Sáez, P., Reyes, I., Valenzuela, C., et al. 2021, AJ, 161, 141
Sanders, N. E., Soderberg, A. M., Gezari, S., et al. 2015, ApJ, 799, 208
Schlegel, D. J., Finkbeiner, D. P., & Davis, M. 1998, ApJ, 500, 525
Schulze, S., Yaron, O., Sollerman, J., et al. 2021, ApJS, 255, 29
Shappee, B. J., Prieto, J. L., Grupe, D., et al. 2014, ApJ, 788, 48
Skilling, J. 2004, in AIP Conf. Ser. 735, Bayesian Inference and Maximum Entropy Methods in Science and Engineering: 24th Int. Workshop on Bayesian Inference and Maximum Entropy Methods in Science and Engineering, ed. R. Fischer, R. Preuss, & U. V. Toussaint (Melville, NY: AIP), 395
Skilling, J. 2006, BayAn, 1, 833
Smith, K. 2019, in The Extragalactic Explosive Universe: The New Era of Transient Surveys and Data-Driven Discovery (Garching: ESO), 51
Sooknunan, K., Lochner, M., Bassett, B. A., et al. 2021, MNRAS, 502, 206
Soraisam, M. D., Saha, A., Matheson, T., et al. 2020, ApJ, 892, 112
Soumagnac, M. T., Ofek, E. O., Liang, J., et al. 2020, ApJ, 899, 51
Sravan, N., Graham, M. J., Fremling, C., & Coughlin, M. W. 2021, arXiv:2112.05897
Sravan, N., Milisavljevic, D., Reynolds, J. M., Lentner, G., & Linvill, M. 2020, ApJ, 893, 127
Street, R. A., Bowman, M., Saunders, E. S., & Boroson, T. 2018, Proc. SPIE, 10707, 1070711
Sukhbold, T., Ertl, T., Woosley, S. E., Brown, J. M., & Janka, H.-T. 2016, ApJ, 821, 38
Szalai, T., & Vinkó, J. 2013, A&A, 549, A79
Tinyanont, S., Kasliwal, M. M., Fox, O. D., et al. 2016, ApJ, 833, 231
Tonry, J. L., Denneau, L., Heinze, A. N., et al. 2018, PASP, 130, 064505
Utrobin, V. P., & Chugai, N. N. 2008, A&A, 491, 507
Utrobin, V. P., & Chugai, N. N. 2009, A&A, 506, 829
Valenti, S., Howell, D. A., Stritzinger, M. D., et al. 2016, MNRAS, 459, 3939
Villar, V. A., Cranmer, M., Berger, E., et al. 2021, ApJS, 255, 24
Villar, V. A., Cranmer, M., Contardo, G., Ho, S., & Yao-Yu Lin, J. 2020, arXiv:2010.11194
Weaver, T. A., Zimmerman, G. B., & Woosley, S. E. 1978, ApJ, 225, 1021
Woosley, S. E., Heger, A., & Weaver, T. A. 2002, RvMP, 74, 1015